

# Quantum simulation of dissipative collective effects on noisy quantum computers

Marco Cattaneo,<sup>1,2,\*</sup> Matteo A. C. Rossi,<sup>3,4</sup> Guillermo García-Pérez,<sup>1,4,5</sup> Roberta Zambrini,<sup>2</sup> and Sabrina Maniscalco<sup>1,3,4</sup>

<sup>1</sup>*QTF Centre of Excellence, Department of Physics, University of Helsinki, P.O. Box 43, FI-00014 Helsinki, Finland*

<sup>2</sup>*Instituto de Física Interdisciplinar y Sistemas Complejos (IFISC, UIB-CSIC), Campus Universitat de les Illes Balears E-07122, Palma de Mallorca, Spain*

<sup>3</sup>*QTF Centre of Excellence, Department of Applied Physics, School of Science, Aalto University, FI-00076 Aalto, Finland*

<sup>4</sup>*Algorithmiq Ltd, Kanavakatu 3C 00160 Helsinki, Finland*

<sup>5</sup>*Complex Systems Research Group, Department of Mathematics and Statistics, University of Turku, FI-20014 Turun Yliopisto, Finland*

Dissipative collective effects are ubiquitous in quantum physics, and their relevance ranges from the study of entanglement in biological systems to noise mitigation in quantum computers. Here, we put forward the first fully quantum simulation of dissipative collective phenomena on a real quantum computer. The quantum simulation is based on the recently introduced *multipartite collision model*, which reproduces the action of a dissipative common environment by means of repeated interactions between the system and some ancillary qubits. First, we theoretically study the accuracy of this algorithm on near-term quantum computers with noisy gates, and we derive some rigorous error bounds which depend on the timestep of the collision model and on the gate errors. These bounds can be employed to estimate the necessary resources for the efficient quantum simulation of the collective dynamics. Then, we implement the algorithm on some IBM quantum computers to simulate superradiance and subradiance between a pair of qubits. Our experimental results successfully display the emergence of collective effects in the quantum simulation. Finally, we analyze the noise properties of the gates we employed in the algorithm by means of full process tomography. Using the state-of-the-art tools for noise analysis in quantum computers, we obtain the values of the average gate fidelity, unitarity and diamond error, and we establish a connection between them and the accuracy of the experimentally simulated state. Although the scaling of the error as a function of the number of gates is favorable, we observe that reaching the threshold for quantum fault tolerant computation is still orders of magnitude away.

## I. INTRODUCTION

Quantum simulation, i.e., the groundbreaking idea of simulating complex quantum systems on a controllable physical platform following the laws of quantum mechanics [1], is probably the most promising application of quantum computers in the near future [2], owing to its exponential quantum advantage [3] which would lead to crucial achievements in both fundamental and applied science [2]. Quantum simulation of unitary many-body systems has been studied and experimentally implemented on several physical platforms [2, 4], including superconducting quantum circuits [5–8], trapped ions [9–11], photonic systems [12] and cold atoms [13, 14]. A relatively less studied problem is the quantum simulation of open quantum systems, whose evolution is not unitary due to the action of an external environment [15–17]. Different protocols for open system quantum simulation have been introduced in the past twenty years [18–32], and careful studies of the resources they require are available in the literature [22, 24, 25, 28, 29, 31]. On the experimental side, the main achievements include the simulation of a quantum map through quantum gates be-

tween trapped ions [33, 34], of different single- and two-qubit quantum channels on a near-term quantum computer [35], of a single-qubit master equation via Trotterization in a superconducting quantum circuit [36], of the Hubbard model with local dissipation on a near-term device [37], and of a single-qubit decay via quantum imaginary time evolution on a near-term computer [32]. In this work, we present the first fully quantum digital simulation of dissipative collective effects on a real quantum computer, reproducing the dynamics driven by a *global* master equation [38–40] due to a common environment acting on the whole system.

Quantum noise is generally considered detrimental for quantum technologies, because it inevitably induces decoherence on the system, hindering the realization of accurate quantum algorithms [41]. Therefore, experimentalists usually try to reduce or counter dissipative processes in quantum computers. Here, our focus is different: we aim to *engineer* the most general coherent processes that occur in a noisy global dynamics. The importance of engineered collective dissipation is broad for both fundamental physics and quantum technologies. Simulating collective dissipation in a qubit platform paves the way for the experimental study of cutting-edge physical phenomena such as dissipative phase transitions [42], quantum synchronization [43–45] and dissipative time crystals [46]. Moreover, such quantum simulations are an

\* marco.cattaneo@helsinki.fi

ideal experimental test-bed for quantum thermodynamics, owing to the importance that global (i.e., collective) master equations have in this field [38–40]. Indeed, it has been shown that local master equations may break the second law of thermodynamics [47], or modify the related energy contributions [48]. Engineered dissipation can also be used to build a different model of universal quantum computation [49], or to generate exotic entangled states by means of a common environment [50–52]. In addition, collective phenomena are believed to play a major role in the dynamics of light-harvesting complexes [53], therefore engineering global master equations may shed new light on the relation between dissipative quantum physics and biological systems. Last but not least, simulating collective dissipation would help to detect and understand cross-talks in quantum computers [54, 55], which may be one of the major sources of noise therein.

In this article, we investigate theoretically and experimentally one of the most well-known dissipative collective processes, namely, the emergence of superradiance [56] and subradiance [57] between qubits emitting simultaneously into a common environment. For this purpose, we use a quantum algorithm recently introduced by some of us, namely the *multipartite collision model* (MCM) [31]. The algorithm reproduces the global emission by means of repeated interactions between the system qubits and a single ancillary qubit that mediates the collective decay. Collision (or repeated interactions) models are an important tool in the theory of open quantum systems [58, 59], with fundamental applications in quantum thermodynamics [48, 60, 61] and in the study of non-Markovianity [62, 63]. Our work is the first implementation of the MCM on a real quantum computer, and one of the first experimental realizations of a collision model [35, 64]. The platforms we have used are some near-term IBM superconducting quantum computers [65].

Current quantum computers are limited by non-negligible gate errors and short coherence time, which impose strong limitations on the depth of quantum circuits. Hence, it is critical to analyze their limitations, identify possible improvements, and characterize their errors [66]. For this reason, a considerable part of our work is devoted to studying, both theoretically and experimentally, the errors arising from noisy gates. On the theoretical side, we estimate a rigorous error bound for the precision of the multipartite collision model. On the experimental side, we perform process tomography of all the gates employed in the algorithm, and state tomography of the system qubits at each step of the quantum simulation. This allows us to better understand the type of noise affecting the quantum devices used in the experiments and to propose possible countermeasures.

A crucial aspect of our analysis is the choice of the figures of merit to estimate the noise properties. The nominal gate errors provided by IBM for all its devices are obtained through a protocol called *randomized benchmarking* [67–72], aimed at estimating the *average gate fidelity* [41]. We compare this quantity with the aver-

age gate fidelity that we obtain from experimental gate process tomography, showing that in some cases the two values do not coincide.

Finally, motivated by the first experiments on quantum advantage [73, 74], we assess the possibility for fault-tolerant quantum computation [41] on the used platforms. The *diamond norm* [75, 76] is the figure of merit most used in the literature to estimate the gate error threshold for fault-tolerance. Using the diamond distance between the ideal and noisy gates employed in our algorithm, we show that the errors in the current devices are still orders of magnitude away from such threshold.

The paper is structured as follows. In Sec. II we introduce the most important theoretical tools to estimate the distance between quantum channels and the errors on a quantum computer. We also discuss the properties of the figures of merit used in our study and compare them. In Sec. III we briefly recall the multipartite collision model and the dissipative quantum dynamics we aim to simulate. Sec. IV is devoted to the discussion of the new theoretical error bounds for the quantum simulation of open systems with noisy gates. In Sec. V we present in detail our experimental results and the noise analysis. Finally, in Sec. VI we draw some concluding remarks and discuss the importance and significance of our results.

## II. ERROR ESTIMATION IN QUANTUM SIMULATION

The goal of quantum simulation is to reproduce any quantum dynamics by means of a suitable composition of quantum channels that we can easily implement on a quantum computer. Therefore, errors in quantum simulation algorithms arise from the difference between such ideal quantum channels and the physical ones implemented in practice. In this section, we introduce some measures to quantify the distance between two quantum channels, in order to provide a precise estimate of the error of a quantum simulation algorithm. Specific emphasis is given to the distance between the ideal quantum gate of our theoretical algorithm and its noisy version, i.e., the actual gate implemented on the quantum computer.

We consider quantum channels  $\mathcal{T} : \mathcal{B}(\mathcal{H}) \rightarrow \mathcal{B}(\mathcal{H})$ , with  $\mathcal{B}(\mathcal{H})$  the space of bounded operators on the Hilbert space of the qubits. According to their usual definition, quantum channels are completely positive, linear, trace preserving maps [15, 41, 76].

### A. Distances between quantum channels and their properties

In this section we introduce the figures of merit for estimating the distance between two quantum channels. These are based either on the “average” or on the “worst-case” scenario [77]. Throughout the paper we will also

employ the trace norm  $\|\cdot\|_1$  and the infinity norm  $\|\cdot\|_\infty$ , which are recalled in Appendix A.

**Definition 1** (Average gate fidelity). If  $\mathcal{U}_g$  is the (ideal) unitary superoperator associated with a quantum gate, and  $\mathcal{T}$  is its noisy implementation, the average gate fidelity is defined as:

$$\begin{aligned} \varphi(\mathcal{U}_g) &= \int d\mu(\psi) \mathcal{F}(\mathcal{U}_g[|\psi\rangle\langle\psi|], \mathcal{T}[|\psi\rangle\langle\psi|]) \\ &= \int d\mu(\psi) \langle\psi|\mathcal{U}_g^{-1}\mathcal{T}[|\psi\rangle\langle\psi|]|\psi\rangle, \end{aligned} \quad (1)$$

where  $d\mu(\psi)$  is the Haar measure over the pure states of the Hilbert space and  $\mathcal{F}$  is the fidelity between two quantum states introduced in Appendix A. Note that if we average over the mixed states instead of pure states we obtain the same result, given the linearity in the definition of a density matrix [77] and the convexity of the infidelity [76].

The average gate fidelity can be estimated, under certain assumptions, employing randomized benchmarking protocols [67–72] which do not require full-state tomography, nor a precise control over the preparation and/or measurement errors. The core idea of these protocols is to apply a random sequence of gates composed with its conjugate transpose on the selected qubits, so that, if the gates were ideal, the outcome channel would be equal to the identity. The “survival probability” of an initial state under this kind of evolution is then computed as a function of the number of gates in the sequence, and an average gate error is estimated by properly fitting the results.

**Definition 2** (Induced superoperator norm). The  $1 \rightarrow 1$  superoperator norm of a quantum channel  $\mathcal{T}$  is defined as:

$$\|\mathcal{T}\|_{1 \rightarrow 1} = \max_{\|\rho\|_1=1} \|\mathcal{T}[\rho]\|_1. \quad (2)$$

The  $1 \rightarrow 1$  superoperator norm has the drawback of being based on the trace norm (see Eq. (A2) in Appendix A), which does not behave well with respect to the tensor product. For this reason, a different norm is usually employed in quantum error correction algorithms:

**Definition 3** (Diamond norm). The diamond norm of a quantum channel  $\mathcal{T}$  is defined as [76, 78]:

$$\|\mathcal{T}\|_\diamond = \|\mathcal{T} \otimes \mathbb{I}_A\|_{1 \rightarrow 1}, \quad (3)$$

where  $\mathbb{I}_A$  is the identity superoperator over a copy of the space  $\mathcal{B}(\mathcal{H})$ .

Note that both the  $1 \rightarrow 1$  and the diamond norms are sub-multiplicative. Furthermore, the diamond norm satisfies the fundamental *stability* property, i.e.,  $\|\mathcal{T} \otimes \mathbb{I}_B\|_\diamond = \|\mathcal{T}\|_\diamond$ , where  $\mathbb{I}_B$  is the identity superoperator over a generic space. Specifically, it can be shown

that the diamond norm defined with the identity superoperator over a copy of the space  $\mathcal{B}(\mathcal{H})$  is the maximal one (it is lower for lower dimensions, and it has the same values for higher dimensions). The diamond norm can be computed either through convex optimization procedures [79] or by a semidefinite program [80, 81].

The diamond distance between an ideal gate with channel  $\mathcal{U}_g$  and its noisy realization  $\mathcal{T}$  is defined as:

$$d_\diamond(\mathcal{U}_g, \mathcal{T}) = \frac{1}{2} \|\mathcal{U}_g - \mathcal{T}\|_\diamond. \quad (4)$$

The sub-multiplicativity of the diamond norm implies that:

$$\|\mathcal{U}_1\mathcal{U}_2 - \mathcal{T}_1\mathcal{T}_2\|_\diamond \leq \|\mathcal{U}_1 - \mathcal{T}_1\|_\diamond + \|\mathcal{U}_2 - \mathcal{T}_2\|_\diamond, \quad (5)$$

and analogously for the  $1 \rightarrow 1$  superoperator norm. This is the *sub-additivity* property, which is crucial to guarantee that the error in the gate composition scales at most linearly as a function of the length of the gate sequence.

Note that both the  $1 \rightarrow 1$  and the diamond norm do not have a closed form as a function of the Choi matrix of the quantum channel we are interested in, but must be computed through numerical maximization. Moreover, unlike the average gate fidelity, they are sensitive to the readout and preparation errors. That is to say, they rely on the precision of the tomographic measurement. A different figure of merit for the distance between quantum channels has been very recently introduced [82].

Finally, we introduce a figure of merit to estimate the *coherence of noise* [83]. That is, how close a given quantum channel  $\mathcal{T}$  is to a unitary one. This will be crucial to understand whether the error of a noisy quantum gate will be mostly due to the presence of decoherence or to the fact that we are performing a gate which is different from the target gate (say, we perform a qubit rotation driven by  $\sigma_x$  instead of the desired  $\sigma_z$ ).

**Definition 4** (Unitarity). The unitarity of a quantum channel  $\mathcal{T}$  is defined as the average purity of output states, with the identity components subtracted:

$$u(\mathcal{T}) = \frac{d_S}{d_S - 1} \int d\mu(\psi) \text{Tr} \left[ \mathcal{T} \left[ |\psi\rangle\langle\psi| - \frac{\mathbb{I}_S}{\sqrt{d_S}} \right]^2 \right], \quad (6)$$

where  $d_S$  is the dimension of the system Hilbert space.

Equivalently, the unitarity can be defined as [83]

$$u(\mathcal{T}) = \frac{1}{d_S^2 - 1} \text{Tr}[\mathcal{T}_u^\dagger \mathcal{T}_u], \quad (7)$$

where  $\mathcal{T}_u$  is implicitly defined by the Liouvillian representation of the channel

$$\mathcal{T} = \begin{pmatrix} 1 & 0 \\ 0 & \mathcal{T}_u \end{pmatrix}. \quad (8)$$

In Eq. (8), the 1 in the diagonal refers to the identity being mapped to itself.

The unitarity of a general quantum channel satisfies  $u(\mathcal{T}) \leq 1$ , being one only if  $\mathcal{T}$  is unitary. Moreover,  $u(\mathcal{V}\mathcal{T}\mathcal{U}) = u(\mathcal{T})$  for all  $\mathcal{U}, \mathcal{V}$  unitary.

## B. Comparing different figures of merit

It is a well-known fact that the fidelity is a deceptive measure to compare quantum states. For instance, the fidelity between states with very different properties, e.g., one entangled and the other separable, can be larger than 0.95 [84]. This is a consequence of the infidelity not being a proper mathematical distance. If we compare it to a well-defined distance such as the trace norm, a common inequality reads [76]:

$$1 - \mathcal{F}(\rho, \sigma) \leq \frac{1}{2} \|\rho - \sigma\|_1 \leq \sqrt{1 - \mathcal{F}(\rho, \sigma)}, \quad (9)$$

where, crucially, the trace norm is bounded by the square root of the infidelity. This means that states with fidelity 0.99 may have a trace distance equal to 0.1.

We can expect similar considerations also when the fidelity is employed to estimate the distance between quantum channels, as in Eq. (1). Indeed, the most important and rigorous theorems guaranteeing fault-tolerant quantum computation do not rely on the fidelity, and instead make use of the diamond distance to bound the maximal error which can be cast away by means of quantum error correction protocols [75, 85–87]. The diamond norm is preferred to the  $1 \rightarrow 1$  superoperator norm because of its stability property, discussed in the previous section. Moreover, addressing the worst case scenario (i.e., performing a maximization as in Eq. (3)) is necessary to estimate a proper fault-tolerant error threshold, while one cannot rely on the average figure of merit in Eq. (1).

An upper bound for the diamond distance as a function of the system dimension  $d_S$  and the average gate fidelity  $\varphi(\mathcal{U}_g)$  is given by [72]:

$$\frac{1}{2} \|\mathcal{U}_g - \mathcal{T}\|_{\diamond} \leq d_S \sqrt{(1 + d_S^{-1})(1 - \varphi(\mathcal{U}_g))}. \quad (10)$$

Once again, we see that the square root of the average gate fidelity appears in the bound. Moreover, the dependency on the system dimension makes its scaling even worse than in Eq. (9). The tightness of this bound has not been proven, but some results indicate that the bound is asymptotically tight as a function of  $\varphi$  and  $d_S$  [86]. They also show how, in general, the average gate fidelity is not reliable for assessing fault-tolerant quantum computation: a value of  $\varphi(\mathcal{U}_g) = 99\%$  can still lead to an error  $\epsilon = 0.45$ , which is very far from the fault-tolerant thresholds (typically  $\epsilon \approx 10^{-2} - 10^{-4}$ ).

To conclude, the diamond norm is the only reliable figure of merit for estimating the distance between quantum gates with the aim of assessing fault-tolerance of the quantum computation, and the values of the average gate fidelity must be taken with a grain of salt (more discussions can be found in Refs. [72, 83, 86–88]). Despite these considerations, most of the experimental results on fault-tolerant quantum computation only report the value of the average gate fidelity via randomized benchmarking or similar figures of merit [89, 90]. In contrast, single-qubit gates achieving the fault-tolerant threshold based

on the diamond norm have been proven in Ref. [91]. The same result for two-qubit gates, to the best of our knowledge, has never been obtained, and can be considered as the next, crucial step toward fault-tolerant quantum computation.

We conclude this section discussing unitarity. This figure of merit can be employed in a quite cumbersome way to estimate some additional bounds connecting infidelity and diamond distance [87, 88]. More importantly for our purposes, it can be used to estimate how the average gate fidelity of composed channels behaves as a function of the average gate fidelity of each component [92], or equivalently, how the average gate fidelity scales as a function of the number of gates in the algorithm.

Without getting into the details discussed in Ref. [92], if we consider, for simplicity, a circuit made of  $m$  identical gates with average gate fidelity  $\varphi$ , then the average gate infidelity of the whole circuit will be bounded by  $m^2(1 - \varphi)$ , plus some lower-order terms that scale as  $m^4(1 - \varphi)^2$  [93]. This bound is tight for all unitary channels with unitarity  $u = 1$ . If, on the contrary, one considers highly incoherent channels, such as the depolarizing one, the bound can be improved as  $m(1 - \varphi)$ , plus terms of the order of  $O(m^2(1 - \varphi)^2)$ . To summarize, lower unitarity implies a better scaling of the infidelity as a function of the channel length.

## III. MULTIPARTITE COLLISION MODEL FOR DISSIPATIVE COLLECTIVE EFFECTS

### A. Introduction to the algorithm

The multipartite collision model (MCM) has been recently introduced [31] as a repeated interaction model [58, 59] able to reproduce any Markovian evolution of a multipartite open quantum system (that is, an open system made of multiple subsystems) by elementary collisions between each subsystem and some environment particles, termed as “ancillas”. Collision models such as the MCM are naturally suited to implement digital quantum simulations of open quantum dynamics. Specifically, we consider a quantum system living in a Hilbert space  $\mathcal{H}$  composed of  $M$  subsystems, which, without loss of generality, we consider identical and of dimension  $d$ :

$$\mathcal{H} = \bigotimes_{j=1}^M \mathcal{H}_j, \quad \dim(\mathcal{H}_j) = d \quad \forall j. \quad (11)$$

We are interested in the most general Markovian quantum evolution of the state of the system at time  $t$ ,  $\rho_S(t)$ . Specifically, starting from a generic  $\rho_S(0)$ , we aim to simulate the dynamics

$$\rho_S(t) = \exp \mathcal{L}t[\rho_S(0)] \quad (12)$$

on a quantum computer, with  $\mathcal{L}$  is the so-called Liouvillian superoperator, i.e., the generator of the quantum dy-

namical semigroup driving the dynamics. The most general structure of the Liouvillian is expressed by the celebrated Gorini-Kossakowski-Sudarshan-Lindblad (GKLS) master equation [15]:

$$\mathcal{L}[\rho_S(t)] = \frac{d}{dt}\rho_S(t) = -i[H_S, \rho_S(t)] + \mathcal{D}[\rho_S(t)], \quad (13)$$

where we are working with units such that  $\hbar = 1$ .  $H_S$  is a generic Hermitian operator of the system, to which we refer as the “effective Hamiltonian”, while

$$\mathcal{D}[\rho_S] = \sum_{k=1}^J \Gamma_k \left( L_k \rho_S L_k^\dagger - \frac{1}{2} \{L_k^\dagger L_k, \rho_S\} \right) \quad (14)$$

is the dissipator, describing the non-unitary system dynamics.  $\Gamma_k \geq 0$  are non-negative decay rates, while  $\{L_k\}_{k=1}^J$  are the Lindblad operators, whose number  $J$  is bounded as  $J \leq d^{2M} - 1$ .

The multipartite collision model provides a way to simulate Eq. (12) on a quantum computer by expressing the action of the dissipator of Eq. (14) in terms of elementary quantum gates between each subsystem, i.e., a subset of qubits, and a collection of ancillary qubits, representing the environment ancillas. Dissipative collective effects, due to terms in Eq. (14) that couple two or more subsystems, are implemented via a suitable sequence of quantum gates between a single environment ancilla and two or more system qubits. More precisely, collective terms are treated through a second-order Suzuki-Trotter decomposition [94]. A detailed presentation of the MCM algorithm is summarized in Appendix B.

The fundamental result introduced in [31] states that the MCM simulates the exact open system dynamics driven by  $\mathcal{L}$  (Eq. (12)) in the limit of small timestep  $\Delta t$ :

$$\lim_{\Delta t \rightarrow 0^+} (\phi_{\Delta t})^n = \exp \mathcal{L}t, \quad n = t/\Delta t, \quad (15)$$

where  $\phi_{\Delta t}$  is the quantum channel reproducing a single step of the MCM (see Appendix B for details), which here has been applied  $n$  times (i.e.,  $n$  repeated collisions until time  $t = n\Delta t$ ).

On a real quantum computer, obviously one can not employ an infinitesimal timestep  $\Delta t \rightarrow 0^+$  to implement the gates in Eq. (B2), and has to choose a small but finite  $\Delta t$ . This implies that the multipartite collision model is able to simulate the dynamical semigroup as in Eq. (15) up to an error which depends on  $\Delta t$ . Let us term this global error as  $\epsilon_g$ , following the original paper [31]:

$$\epsilon_g = \|(\phi_{\Delta t})^n - \exp \mathcal{L}t\|_{1 \rightarrow 1}. \quad (16)$$

The global error can be trivially bounded by the sum of the errors in a single timestep:  $\epsilon_g \leq n\epsilon_s$ , where

$$\epsilon_s = \|\phi_{\Delta t} - \exp \mathcal{L}\Delta t\|_{1 \rightarrow 1}. \quad (17)$$

Ref. [31] estimates a very general bound on  $\epsilon_s$ , showing that its scaling is optimal for collision models. This

allows for the efficient implementation of the quantum simulation algorithm. The complete expression of this bound is quite cumbersome and can be found in the Supplemental Material of Ref. [31]. Here, we just write it as:

$$\begin{aligned} \epsilon_s &\leq \mathcal{B}_{1 \rightarrow 1} \\ &= 2e(M\Lambda(1 + JRA)\Delta t)^2 \\ &\quad + \text{pol}_1(\Lambda, M, J)\Delta t^2 + \text{pol}_2(\Lambda, M, J)\Delta t^3, \end{aligned} \quad (18)$$

where  $\Lambda = \max_{k,m} \{ \|H_S\|_\infty, \|(\lambda_k F_m^{(k)} \sigma_k^+ + h.c.)\|_\infty \}$  (the latter term being the Hamiltonian driving a single collision, as explained in Appendix B), and  $\text{pol}_1$  and  $\text{pol}_2$  are polynomial functions of  $\Lambda$ , the number of subsystems  $M$ , and the maximum number of jump operators  $J$ . The scaling of the global error is  $\epsilon_g \sim O(n\Delta t^2) = O(t^2/n)$ . Finally, note that  $J$  scales exponentially with the number of subsystems. However, under the very common assumption of  $k$ -locality [3, 22], i.e., the jump operators and the effective Hamiltonian can be decomposed as sums of  $k$ -local terms which act non-trivially on  $k$  subsystems only, the bound in Eq. (18) scales polynomially as a function of  $M$  [22, 31]. This guarantees that the multipartite collision model is efficiently simulable on a quantum computer.

## B. Simulation of super- and sub-radiance

We will now show how the multipartite collision model can be applied to the simulation of topical collective effects, such as super- and sub-radiance. The simplest model where these phenomena arise consists of two atoms that emit coherently into a common environment. Specifically, superradiance emerges when the atoms lose their energy through a quick emission, the intensity of which is enhanced with respect to the local incoherent decay that each atom would experience in the absence of the other [56]. In contrast, subradiance, which is a complementary effect due to same cause (namely, the action of a common bath), can be identified as the presence of a slowly decaying, metastable mode of the atomic emission, which persists for a time way longer than the usual relaxation time [57] ( $T_1$  in the language of cavity or circuit quantum electrodynamics [8]).

In this work we address super- and sub-radiance between two two-level atoms, i.e., two qubits of a quantum computer. Despite its simplicity, this model displays a rich landscape of collective phenomena [95] that may also bring new insights on the presence of entangling noise in the experimental platform [96]. Remarkably, we will address a scenario where subradiance emerges through the presence of a decoherence-free subspace, that is, a subspace of the system Hilbert space where the dynamics is unitary and there is no dissipation. The relevance of decoherence-free subspaces for quantum computation is crucial, given that noiseless computation may be possible by restricting the Hilbert space over which we run

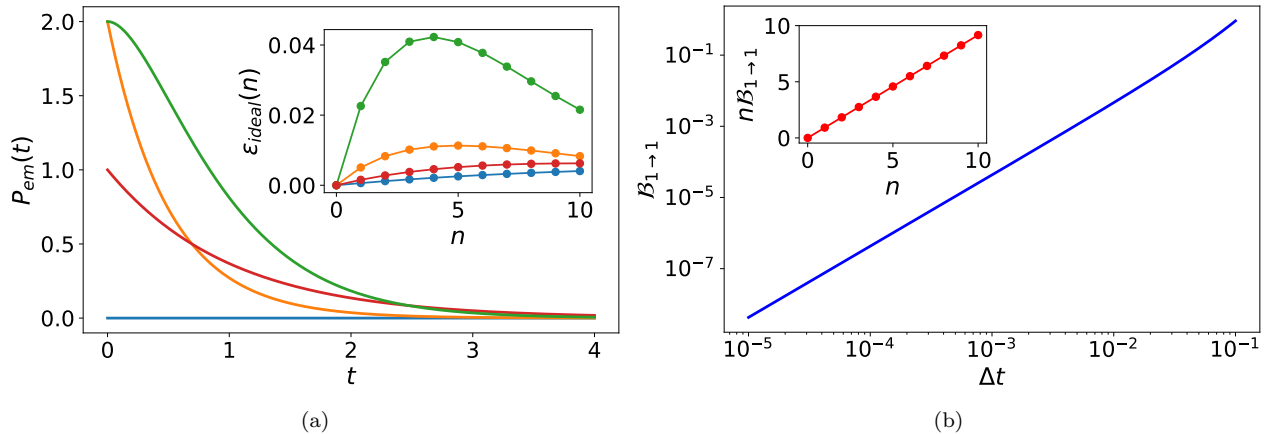


FIG. 1: (a): Emission power as a function of time, when the initial state is the subradiant state (blue), superradiant state (orange),  $|ee\rangle$  (green), and when the dynamics is local starting from the subradiant state (red). Inset in (a): Trace distance between real and simulated state  $\epsilon_{ideal}(n)$  as a function of the number of timesteps  $n$ , with the same initial states as in the main figure. (b): Upper bound  $B_{1 \rightarrow 1}$  for the single-step error  $\epsilon_s$  as a function of the timestep  $\Delta t$ . Inset in (b): Upper bound for the global error  $\epsilon_g$  with  $\Delta t = 0.1$ , equal to  $n$  times  $B_{1 \rightarrow 1}$ , where  $n$  is the number of timesteps.

the quantum algorithms to the decoherence-free subspace [97]. More specifically, we aim to simulate the following generator of the open system dynamics:

$$\begin{aligned} \mathcal{L}[\rho_S] &= \sum_{j,k=1,2} \gamma \left( \sigma_j^- \rho_S \sigma_k^+ - \frac{1}{2} \{ \sigma_k^+ \sigma_j^-, \rho_S \} \right) \\ &= \gamma \left( L_{col} \rho_S L_{col}^\dagger - \frac{1}{2} \{ L_{col}^\dagger L_{col}, \rho_S \} \right), \end{aligned} \quad (19)$$

with  $L_{col} = (\sigma_1^- + \sigma_2^-)$ , and the latter are the lowering operators of respectively qubit 1 and 2. In Eq. (19)  $\gamma$  is a constant decay rate which defines the magnitude of the dissipation and, specifically, it is the spontaneous emission coefficient of each atom in the vacuum.

The master equation (19) can be derived from a microscopic model with two identical two-level atoms dissipatively coupled in a symmetric way to the same common bath at zero temperature [40]. In a reference frame rotating with the frequency of the qubits, the free Hamiltonian of the atoms can then be neglected, as in Eq. (19). The analytical solution of the dynamics driven by Eq.(19) can be found in Appendix C.

Superradiance is observed when the open evolution of the two qubits starts from the “superradiant state”  $|\psi_{sup}\rangle = \frac{|ge\rangle + |eg\rangle}{\sqrt{2}}$ , where  $|g\rangle$  and  $|e\rangle$  are respectively the ground and the excited state of each qubit. Indeed, introducing  $\rho_{sup} = |\psi_{sup}\rangle \langle \psi_{sup}|$  and the emission power [56]

$$P_{em}[\rho_S(0)](t) = -\text{Tr}[H\mathcal{L}[\exp \mathcal{L}t[\rho_S(0)]]], \quad (20)$$

where  $H = \frac{1}{2}(\sigma_1^z + \sigma_2^z)$  is the system’s energy, we easily find (see Appendix C for details):

$$P_{em}[\rho_{sup}](t) = 2\gamma e^{-2\gamma t}. \quad (21)$$

We observe a clear enhancement of the atomic decay, driven by a decay rate equal to  $2\gamma$  instead of the standard spontaneous emission rate  $\gamma$ .

In contrast, subradiance emerges when the system dynamics starts from the “subradiant state”  $|\psi_{sub}\rangle = \frac{|eg\rangle - |ge\rangle}{\sqrt{2}}$ . Defining  $\rho_{sub} = |\psi_{sub}\rangle \langle \psi_{sub}|$ , we observe

$$\mathcal{L}[\rho_{sub}] = 0, \quad (22)$$

with zero emitted power. In other words, the subradiant state is a steady state of the dynamics that does not “feel” the presence of dissipation acting on the qubits.

Let us now expose how the multipartite collision model can simulate the dynamics in Eq. (19). Since there is a single Lindblad operator ( $J = 1$ ), we only need a single ancillary qubit initialized in the ground state for each timestep  $\Delta t$ . Let us term it as the qubit  $E$ . Then, the two-qubit quantum gates we will employ in the algorithm are:

$$\begin{aligned} U^{(1)}(\Delta t) &= \exp \left[ -i\sqrt{\Delta t}(\sqrt{\gamma}\sigma_1^- \sigma_E^+ + h.c.) \right], \\ U^{(2)}(\Delta t/2) &= \exp \left[ -i\frac{\sqrt{\Delta t}}{2}(\sqrt{\gamma}\sigma_2^- \sigma_E^+ + h.c.) \right]. \end{aligned} \quad (23)$$

These gates will be composed as in Eq. (B2).

Let us also consider the analogous quantum evolution in the presence of two separate baths, i.e., without collective effects between the qubits. Then, the master equation driving this dynamics, assuming once again that the frequencies of the qubits and their decay rates are the same, is equivalent to Eq. (19) without cross terms with  $j \neq k$  in the summation (see Appendix C and Eq. (C10) for further details). In this scenario, we have two local Lindblad operators, namely  $\sigma_1^-$  and  $\sigma_2^-$ . Therefore, the

multipartite collision model to reproduce the local dynamics requires two ancillas, say respectively qubit  $E_1$  and qubit  $E_2$ , and the same gates as in Eq. (23), both lasting for a time  $\Delta t$ . Indeed, in the absence of collective effects we do not need to employ the second-order Suzuki-Trotter decomposition as in Eq. (B2), while we can just rely on its first-order analogous [31, 98].

Let us now fix the values of  $\gamma$  and  $\Delta t$ . We set  $\gamma = 1$  (after choosing some suitable units of measurement), which is the only physical timescale of the problem. This means that thermalization is reached at a time  $t_R \sim O(1)$  [40]. The time evolution of the emission power of Eq. (20) is plotted in Fig. 1(a) for different initial states (superadiant, subradiant, and the excited state  $|ee\rangle$ ), and compared to the case of local dissipation for an initial subradiant state.

For the quantum simulation, we choose  $\Delta t = 0.1$  and consider the dynamics until  $t = 1$ , requiring  $n = 10$  timesteps. The upper bound on the single-step error, given by Eq. (IV), is plotted in Fig. 1(b) as a function of the timestep  $\Delta t$ . These high values of the single-step error are due to the fact that the bound in Eq. (18) reflects the worst-case scenario (the maximization is performed over all the initial states). This is necessary to guarantee the efficiency of the quantum simulation of the algorithm, but quite often of little use for practical purposes. Therefore, in Fig. 1(a) (inset) we plot the trace distance between  $\rho_S(t)$ , as obtained from Eq. (19), and the state simulated by the MCM with  $\Delta t = 0.1$ , as a function of the number of timesteps, i.e.,

$$\epsilon_{\text{ideal}}(n) = \|\exp \mathcal{L}(n\Delta t)[\rho_S(0)] - (\phi_{\Delta t})^n[\rho_S(0)]\|_1, \quad (24)$$

for  $n = 1, \dots, 10$ . Note that  $\epsilon_{\text{ideal}}(n)$  is different from the global error at the  $n$ th timestep  $\epsilon_g$  introduced in Eq. (16). Indeed, in Eq. (24) there is no maximization over all the possible initial states, since we focus on a specific initial state. As a consequence,  $\epsilon_{\text{ideal}}(n)$  is much lower than  $\epsilon_g$ . In fact, in Fig. 1(a) (inset) we observe that, even with a large timestep such as  $\Delta t = 0.1$ , the MCM is able to simulate the state of the dynamics at time  $t$  with high accuracy.

#### IV. ERROR BOUND FOR THE NOISY SIMULATION

In Ref. [31] an error bound for the ideal case of the MCM based on the  $1 \rightarrow 1$  superoperator norm is computed. For a single step of the MCM, it is expressed as in Eq. (18). Here, we estimate an analogous upper bound for the case of noisy gates. We use the diamond norm instead of the  $1 \rightarrow 1$  superoperator norm to obtain bounds expressed in terms of error values that can be employed to guarantee fault-tolerant quantum computation.

Let us first replace the ideal quantum map  $\phi_{\Delta t}$ , defined in Eq. (B5), with a noisy one, which we term as  $\phi_{\Delta t}^*$ . The error we want to estimate is:

$$\epsilon_g^* = \|(\phi_{\Delta t}^*)^n - \exp \mathcal{L}t\|_{\diamond}, \quad \text{with } t = n\Delta t. \quad (25)$$

Thanks to the triangle inequality, we have:

$$\begin{aligned} \epsilon_g^* &\leq \|(\phi_{\Delta t})^n - \exp \mathcal{L}t\|_{\diamond} + \|(\phi_{\Delta t}^*)^n - (\phi_{\Delta t})^n\|_{\diamond} \\ &\leq n(\epsilon_s^{\diamond} + \epsilon_m^*), \end{aligned} \quad (26)$$

where we have introduced the errors

$$\epsilon_s^{\diamond} = \|\phi_{\Delta t} - \exp \mathcal{L}\Delta t\|_{\diamond}, \quad \epsilon_m^* = \|\phi_{\Delta t}^* - \phi_{\Delta t}\|_{\diamond}. \quad (27)$$

Let us focus on these norms for a single application of the MCM. We first address the bound for the ideal case based on the diamond norm  $\epsilon_s^{\diamond}$ , and then the diamond distance  $\epsilon_m^*$  between the ideal and noisy MCM maps. We give here only the final result, while the derivation of the bounds can be found in Appendix D. Our first statement is:

**Proposition 1.** *The ideal error bound  $\mathcal{B}_{1 \rightarrow 1}$  evaluated through the  $1 \rightarrow 1$  superoperator norm as in Eq. (18) is valid also for the diamond norm:*

$$\epsilon_s^{\diamond} \leq \mathcal{B}_{1 \rightarrow 1}, \quad (28)$$

where the expression  $\mathcal{B}_{1 \rightarrow 1}$  was introduced in Eq. (18).

This means that all the results of Ref. [31] about the scaling of the error can be trivially extended to a scenario where the diamond norm is employed. In particular, the efficient quantum simulation of the algorithm is guaranteed also through the diamond norm. Note that, for instance, the behavior of the upper bound shown in Fig. 1(b) holds also for  $\epsilon_s^{\diamond}$ .

Let us now focus on  $\epsilon_m^*$ . Our aim is to estimate “how far” the noisy implementation of the MCM is from its ideal analog. To do so, we may assume that each ancillary qubit is not prepared in the ideal initial state  $\rho_{E,i}$ , but in the noisy  $\rho_{E,i}^* = \mathcal{G}_i[\rho_{E,i}]$ , where  $\mathcal{G}_i$  is a known quantum channel characterizing the noise on the state preparation of the  $i$ th ancilla in the actual device. The quantum channel for the total unitary evolution of the system+ancillary qubits of the ideal MCM for a single timestep  $\Delta t$  is  $\mathcal{U}_{\text{sim}}(\Delta t) = U_{\text{sim}}(\Delta t) \cdot U_{\text{sim}}^{\dagger}(\Delta t)$  (see Eq. (B4)). The unitary evolution  $U_{\text{sim}}(\Delta t)$  can also be decomposed as a composition of many quantum gates on a quantum computer, such as  $\mathcal{U}_{\text{sim}}(\Delta t) = \prod_j \mathcal{U}_j$ . Let us now suppose that, on a real platform, each of these gates is not ideal but noisy, and can be represented by the quantum channel  $\mathcal{E}_j$ . Then, we find:

**Proposition 2.**

$$\begin{aligned} \epsilon_m^* &\leq \sum_j \|\mathcal{E}_j - \mathcal{U}_j\|_{\diamond} + \sum_i \|\mathcal{G}_i - \mathbb{I}_E\|_{\diamond} \\ &= 2 \left( \sum_j d_{\diamond}(\mathcal{U}_j, \mathcal{E}_j) + \sum_i d_{\diamond}(\mathbb{I}_E, \mathcal{G}_i) \right), \end{aligned} \quad (29)$$

where  $\mathcal{G}_i$  and  $\mathcal{E}_j$  are the noisy channels introduced above, while the diamond distance  $d_{\diamond}$  is defined in Eq. (4).

That is to say, even though the MCM map acts on the state of the system only, we can estimate an upper error bound for the noisy map that is equal to the sum of the individual errors for each quantum gate between the system qubits and the ancillas (including the preparation of the initial states of the ancillary qubits). Note that the above error bound is valid also for modified versions of the MCM, where, for instance, the ancillary qubits can be prepared in an initial entangled state. Moreover, the above bound is robust even under more general sources of error, e.g., if the initial state of system qubits+ancillas is accidentally entangled. Indeed, the diamond distance  $\|\mathcal{E}_j - \mathcal{U}_j\|_\diamond$  involves a maximization over all the possible initial states of the overall system, including the entangled ones. In such a scenario, the noisy preparation given by the set of  $\mathcal{G}_i$  can then be extended to act on both system qubits and ancillas, yielding an entangled state instead of an initial state that is separable between system and ancillary qubits.

To summarize, the results stated in Proposition 1 and Proposition 2 can be employed to estimate a general upper bound for the global error of the noisy MCM map, according to Eq. (26). More specifically, Eq. (28) expresses the error due to the finite (and not infinitesimal) timestep  $\Delta t$  in the ideal algorithm. Clearly, the lower  $\Delta t$  the better, as shown in Fig. 1(b). Instead, Eq. (29) states that the error due to a noisy MCM protocol can be decomposed into the sum of the individual errors for each quantum gate employed in the algorithm, including the state preparation of the ancillary qubits.

We stress again that we are using the diamond distance, which is employed to prove the formal theorems about fault-tolerant quantum computation. This means that the distances between noisy and ideal gates that appear in Eq. (29) express exactly the errors that we must keep below a certain threshold to guarantee fault-tolerant computation. Moreover, recall that the diamond norm addresses the worst-case scenario, so the upper error bound can be way higher than the actual error in a single implementation of the algorithm (compare Figs. 1(a) and (b)).

## V. EXPERIMENTAL DEMONSTRATION ON IBM QUANTUM COMPUTERS

In this section, we present the implementation of the multipartite collision model on a near-term superconducting IBM quantum computer available on the cloud, programmed through the library Qiskit [65]. In particular, we will show some experimental results obtained on the limited-access 16-qubit `ibmq_guadalupe`, while more results on the 27-qubit `ibmq_toronto` are discussed in Appendix F. We consider the protocol introduced in Sec. III B for the simulation of super- and sub-radiance, addressing the emission power dynamics for the different cases depicted in Fig. 1(a).

Our aim is twofold. On the one hand, we want to

show how even current near-term devices can display non-trivial collective effects in a quantum simulation. On the other hand, we intend to investigate the properties of noise in these platforms, and to relate them with the accuracy of the simulation of the MCM. Here, we present two different sets of results. The first one shows clear signatures of collective effects, and the accuracy of the simulation is reasonably good. The second one displays noisier results, and the simulated MCM yields results that are quite far from their expected values. We will show, however, that this can be traced back to some highly noisy gates that are repetitively employed in the algorithm, the noise properties of which are captured by our analysis.

The experimental details and the platform schemes can be found in Appendix E. Shortly, the protocols that, for the above-mentioned purposes, we have to run on the devices are (note that tomography is not needed for the MCM, but only to assess errors):

1. Algorithm implementing the MCM until the step  $n = 5$  for the three different initial states explored in Sec. III B and for the local dynamics, and performing measurements in the computational basis.
2. State tomography of the system at each timestep of the algorithm.
3. Process tomography [41] of the CNOT gates employed in the algorithm, in order to estimate the noise properties. We do not address the properties of the single-qubit gates, because their error is usually way lower than the one of two-qubit gates (see Appendix E for further details).
4. Readout error mitigation on the qubits measured in both the algorithm and the gate process tomography. This is a standard procedure that can be implemented on the IBM near-term devices through the Qiskit library [65]. It detects possible systematic errors in the outcomes of the measurements on the set of qubits of interest, and allows for readout error mitigation. All the outcomes we will show in the manuscript have been obtained after applying the proper readout error mitigation procedure.

Note that we will simulate  $n = 5$  steps of the MCM, using the same model parameters that have been employed in Sec. III B (namely, decay rate  $\gamma = 1$ , timestep  $\Delta t = 0.1$ ). The specifics of the near-term devices we are employing and the noise level do not allow for more collisions between the system qubits and the ancillas. In any case, we will see that 5 steps are already enough to observe collective effects in the dynamics.

It is worth stressing that a crucial challenge in the simulation of the MCM is getting a new ancilla initialized in the ground state after each collision, as required by the steps of the algorithm discussed in Appendix B. In general, in the topology of a quantum computer only one or two ancillary qubits are directly connected to (i.e., can



perform operations with) both the system qubits. Therefore, we have generated a new refreshed ancilla after each timestep by swapping the state of the common ancillary qubit with the one of the nearby qubits prepared in the ground state. To do this, we need more and more swap gates as the number of collisions increases, giving rise to a “train of ancillas” that must be subsequently swapped to get to interact with the system qubits. More details can be found in Appendix E. A different solution may consist in employing a reset gate to reinitialize the state of the common ancillary qubit in the ground state after each collision. However, this did not work on the platforms we have used due to decoherence effects, as shown in Appendix F.

## A. Observation of collective effects

### 1. Experimental MCM outcomes

A first set of results and measurement outcomes in the computational basis of the quantum computer is shown in Fig. 2 as a function of the number of steps in the MCM, from  $n = 0$  (state preparation) to  $n = 5$ . The computational basis “00”, “01”, “10”, “11” corresponds to the physical basis  $|gg\rangle$ ,  $|ge\rangle$ ,  $|eg\rangle$ ,  $|ee\rangle$  of the two qubits.

The results display a clear evidence of dissipative collective effects in the system dynamics. For instance, the decay of the experimental subradiant state following the collective dynamics (blue markers) is slower than the theoretical predictions in the case of a local incoherent dynamics (solid red lines), that is, the system is experiencing subradiance. Note that, although the blue markers are below the red solid line in the detection of  $|ge\rangle$ , this is not due to a faster, incoherent decay of the subradiant state, but to an imprecise state preparation at time  $t = 0$ .

It is worth noting, however, that the subradiant state is decaying, while it should be stationary according to the master equation. In other words, there are leakages out of the decoherence-free subspace. This is due to the errors in the gates we employed in the algorithm, which are inevitably noisy in near-term devices. Another source of leakages is due to the finite Trotter timestep  $\Delta t$  of the algorithm. However, as one can see in the inset of Fig. 1(a), the discrepancy between the true dynamics and the ideal simulation is very small, therefore this source of leakages is basically negligible in the present scenario.

We stress that, despite the dissipation due to the gate errors, we have proven that the multipartite collision model produces a more robust subradiant state than in the presence of local decay only. Therefore, our algorithm is able to preserve entanglement between the qubits for a longer time than in the absence of collective effects, even on near-term devices with a considerable level of decoherence.

The superradiant state displays a clear enhanced decay rate in the collective dynamics, at least at the first stages

of the evolution. During the last collisions, decoherence emerges and the quick decay towards the ground state slows down. Note that, again, the major discrepancies between the theoretical and experimental results are due to the imprecise state preparation, while the scaling of the evolution is preserved. In particular, it is evidently much faster than with local dissipation only, and this is yet another clear signature of collective effects in the dynamics. The evolution of the state  $|ee\rangle$  follows the scaling of the theoretical predictions as well. Moreover, it does not run into the error in the state preparation, since preparing  $|ee\rangle$  (starting from  $|gg\rangle$ ) requires only single-qubit gates. In contrast, the initialization of the super- and sub-radiant states involves two-qubit gates, which are much noisier than single-qubit operations, and this is why their state preparation is more imprecise.

### 2. Gate error analysis

Let us now focus on the gate analysis displayed in Fig. 3. In the lower plot, the experimental average gate infidelity of the CNOTs in the algorithm, computed by reconstructing the Choi matrix of the gate [99] through gate process tomography, is compared to the nominal gate error provided by IBM and extrapolated through a randomized benchmarking protocol [65, 69]. We also plot the value of  $1 - u(\mathcal{T})$ , where  $u(\mathcal{T})$  is the unitarity of the noisy gate described by the channel  $\mathcal{T}$ , see Eq. (6). We first make two major remarks:

- (i) The unitarity of each quantum gate decreases as the average gate infidelity increases, with no exception. Indeed, looking at the inset in the lower plot we observe excellent positive correlation between 1-unitarity and average gate infidelity. Hence, the “coherence of noise” [83] in the hardware is quite low, and the dominant source of error is incoherent. This agrees with previous studies on the noise properties of the gate pulses on the IBM quantum computers [100].
- (ii) The experimental average gate infidelity is of the same order of magnitude as the nominal gate error, but, with few exceptions, it is usually slightly higher than the latter. In other words, we are observing a discrepancy between the actual average gate fidelity and the randomized benchmarking value. Similar remarks on the IBM quantum devices can be found in the literature [101, 102]. Moreover, scatterplots analogous to the one in the inset of Fig. 3 for nominal IBM gate error vs average gate infidelity and vs 1-unitarity do not display any clear correlation. Note that the average gate fidelities of a single CNOT and its inverse (e.g., CNOT 0-1 and 1-0) are different. This means that, for each pair of qubits, the physical error may depend on the chosen gate. A rigorous relation between the average gate fidelity and its

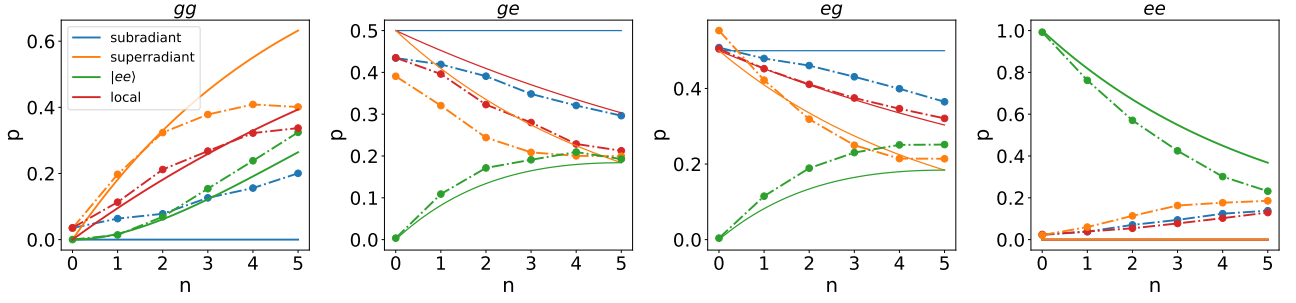


FIG. 2: Probability of finding the states  $|gg\rangle$ ,  $|ge\rangle$ ,  $|eg\rangle$ ,  $|ee\rangle$  (from left to right) through a projective measurement in the computational basis as a function of the number of steps in the MCM (first set of results), when the initial state is the superradiant state (blue), subradiant state (orange),  $|ee\rangle$  (green), and when the dynamics is local starting from the subradiant state (red). Solid lines: theoretical prediction based on the master equation. Markers of the dashed-dotted lines: experimental values. The emergence of collective effects is clear from the dynamics. In particular, the subradiant state following a collective evolution (blue lines) is more robust than with local dissipation only (red lines). The results have been obtained as averages over 37 realizations of the protocol, and the error bars are within the markers.

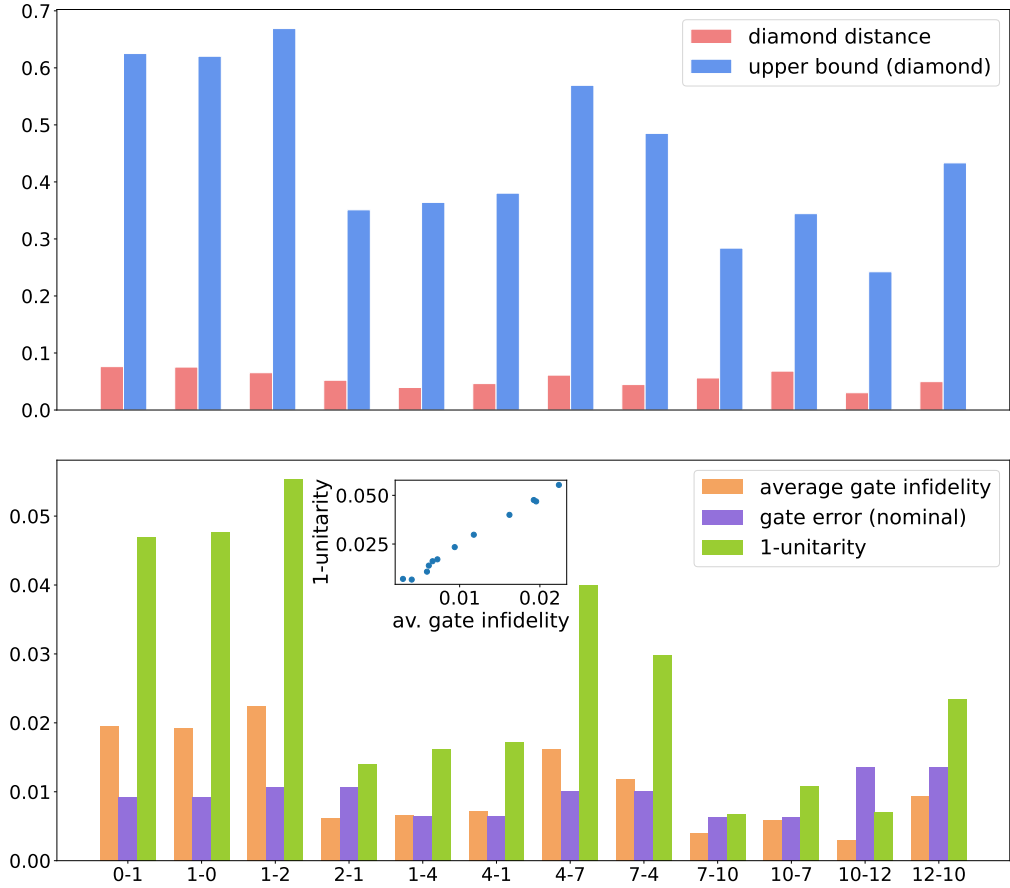


FIG. 3: Error analysis of the set of CNOT gates in `ibmq_guadalupe` employed for the simulation of the results in Fig. 2. The tick 0 – 1 on the x axis corresponds to the CNOT gate where “qubit 0” in `ibmq_guadalupe` is the control qubit and “qubit 1” is the target. Upper plot: diamond distance between ideal and noisy CNOT according to Eq. (4) (light red), and corresponding upper bound based on the average gate fidelity (light blue), as defined in Eq. (10). Lower plot: experimental average gate infidelity  $1 - \varphi(\mathcal{U}_g)$  introduced in Eq. (1) (orange), nominal average gate infidelity obtained through randomized benchmarking (purple) and  $1 - u(\mathcal{T})$  (green), where  $u(\mathcal{T})$  is the unitarity of the noisy gate, defined in Eq. (6). Inset: scatterplot with 1-unity vs average gate infidelity.

randomized benchmarking value is, to the best of our knowledge, known only for gate-independent noise [68, 103]. A similar relation which makes use of the *gate-set circuit fidelity* (average over the average gate fidelities of a gate set) is known for gate-dependent noise of high-fidelity gates [103–105]. Our findings, however, suggest that the randomized benchmarking procedure employed by IBM may not always be reliable to estimate the average gate fidelity of each circuit CNOT, possibly due to some complex physical error on the backend.

Note that the discrepancy between the experimental gate fidelity and the nominal gate error can hardly be explained by possible preparation and readout errors that may affect the experimental value. Indeed, the state preparation for the process tomography of the CNOTs involves only single-qubit gates and, as observed for the state preparation of  $|ee\rangle$ , these display very low levels of noise. Moreover, readout error mitigation has been applied to all the results in Fig. 3. Without error mitigation, the experimental average gate infidelities would be huge. So, it is reasonable to assume that the readout errors have been mostly swept away by the mitigation procedure.

Furthermore, we would like to stress that this discrepancy cannot be traced back to a “gauge error” in the gate implementation. Randomized benchmarking is known to give a wrong estimation of the average gate fidelity in the presence of some kind of coherent errors [106, 107]. This is basically due to a gauge freedom in the definition of the gates [105]: if our experimental gate is actually implementing  $\sigma_x$ , while our aim is to run  $\sigma_z$  (and so on for all the Pauli matrices), then we obtain a very low average gate fidelity, while randomized benchmarking detects no errors ( $\sigma_z$  is still unitary). However, we observe that, when there is a notable discrepancy between the experimental infidelity and the nominal gate error (for instance, consider the CNOTs 0-1, 1-0 and 1-2 in Fig. 3), the unitarity of the error considerably decreases as the error increases. In other words, some source of incoherent noise is responsible for the experimental infidelity being so high, and the presence of a gauge error must be discarded.

Finally, let us consider the upper plot in Fig. 3, which depicts the diamond error of each CNOT. Note that these diamond distances are exactly the ones appearing in the bound in Proposition 2, Eq. (29). That is, they can be used to estimate the simulation error of the MCM due to its noisy implementation. Moreover, the diamond distance between the ideal and the experimental gate of a quantum computer is the key figure of merit for estimating the error rates in quantum fault tolerant theorems [75]. We can make two conclusive remarks:

- (iii) We observe that the experimental diamond distances for the noisy CNOTs are between  $5 \times 10^{-2}$  and  $10^{-1}$ . As the largest rigorously established threshold values for efficient quantum-error-

correcting codes are of the order of  $10^{-3}$  [86], we can safely claim that, for this kind of near-term devices, fault-tolerant quantum computation is still orders of magnitude away. As a consequence of the very high diamond distances, the rigorous error bound for the MCM in Eq. (29) gives a value that quickly exceeds 1.

- (iv) Fig. 3 also plots the upper bound for the diamond distance based on the average gate fidelity, as expressed in Eq. (10). We observe that the upper bound is typically around 10 times higher than the actual diamond distance. This bound was conjectured to be tight in Ref. [86]. However, our results do not even get close to it. This may be due to the fact that, as shown in the lower plot of Fig. 3, the errors are mostly due to decoherence effects. In contrast, higher values of the diamond distance for the same average gate fidelity are obtained with coherent errors, the unitarity of which approaches 1 [86, 87].

### 3. Scaling of the experimental infidelity

Fig. 4 depicts the infidelity and the trace distance between the ideal and experimental states as a function of the number of gates in the protocol  $\mathcal{N}_g$ , during the simulation of different collective effects for the first set of results. The markers indicate the state at each step of the algorithm, from  $n = 0$  (state preparation) to  $n = 5$ . Note that the number of gates to implement the  $n$ th step is higher than for the step  $n - 1$ , as explained in Appendix E. In Fig. 4, we also plot the average channel infidelity of the overall protocol, under the assumption that it is just given by the linear sum of the average gate infidelities of all the CNOTs employed in the algorithm, taking into account their repetitions, and following the order in which they appear in the circuit (i.e.,  $\mathcal{N}_g = 1$  on the  $x$  axis denotes the first gate we employ in the algorithm, and so on). We plot this linear scaling for both the experimental average gate infidelity obtained through gate process tomography and the nominal gate error provided by IBM, which are displayed in Fig. 3. Note that these curves are not exactly straight lines, because the average gate fidelities of the gates employed in the algorithm are in general different.

According to the discussion in Sec. II B, we expect the experimental state infidelity to scale linearly when the noise source is mostly incoherent [87, 92]. We indeed observe a linear scaling, or also sublinear, as a function of the number of gates. The linear sum of the experimental average gate infidelities captures well the first stages of the algorithm, but then overestimates the error. This may suggest that, in the platform we are considering, the average gate fidelity of composed channels [92] scales in a favorable way, which may also be sublinear. We remark, however, that for the high values of infidelities

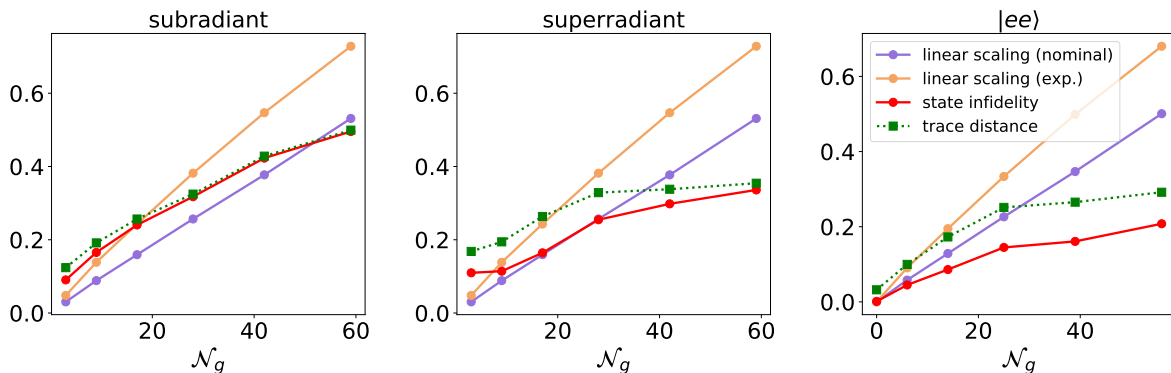


FIG. 4: Scaling of the error as a function of the number of gates in the algorithm  $\mathcal{N}_g$  during the simulation of the collective dynamics displayed in Fig. 2. The markers indicate the steps of the collision model. Solid orange and solid purple lines: linear scaling of respectively the experimental and the nominal average gate fidelity, given in Fig. 3.

Solid red line: experimental infidelity between the simulated state and the ideal one. Dotted green line: experimental trace distance between the simulated state and the ideal one. Both quantities display a linear or sublinear scaling as a function of  $\mathcal{N}_g$ .

obtained at the later stages of the algorithm, we must expect a sublinear scaling, because the infidelity cannot be larger than 1. Remarkably, a similar behavior is found for the trace distance also, which, in general terms, might display a worse scaling than the infidelity.

### B. Detrimental effects of noise

In this section, we will focus on the second set of results on the implementation of the MCM on `ibmq_guadalupe`. We will observe how a pair of very noisy gates can jeopardize the simulation of collective effects on near-term devices.

The outcomes of the measurements in the computational basis at each step of the algorithm are shown in Fig. 5. It is quite evident that the results are very noisy, and almost no signature of collective effects can be extrapolated from them. In particular, the experimental evolution of the subradiant state following the collective dynamics (blue markers) shows no slower decay than in the case of local dissipation only (solid red lines). The superradiant state does display a fast (although not always accurate) decay during the first two collisions, but decoherence gains the upper hand starting from the third one, and the dynamics stabilizes at a wrong value. The concavity of the evolution of  $|ee\rangle$  is often erroneous as well.

The gate analysis in Fig. 6 sheds light on the origin of these noisy results. We have found an experimental average gate infidelity of the CNOTs 1-2 and 2-1, which are repetitively employed in the algorithm, as explained in Appendix E, considerably higher than its nominal value obtained through randomized benchmarking. These gates are responsible for the noisy dynamics in Fig. 5, as can be deduced from Fig. 7: the state infidelity as a function of the number of gates is well captured by

the linear scaling of the experimental average gate infidelities of the CNOT gates (see the discussion on the first set of results for further details). In particular, the mismatch between ideal and noisy state preparation of the super- and sub-radiant states is detected by the experimental gate infidelity only. For the state  $|ee\rangle$ , we do not observe such a discrepancy, because the CNOTs are not employed in the state initialization. After some collisions, the state infidelity shows a sublinear scaling, as for the first set of results. Analogously, this may be explained by the fact that the infidelity must scale sublinearly as a function of  $\mathcal{N}_g$  when its value gets high, because it can never exceed 1.

As was also observed for the first set of results, the gate analysis in Fig. 6 suggests that computing the average gate fidelity through process tomography is generally more reliable than randomized benchmarking on the IBM devices which we employed. Even more clearly, the noisy outcomes of the second set of results in Fig. 5, and the state preparation together with the first collisions in Fig. 7, are a strong evidence of how inaccurate the quantum simulation can be as a consequence of highly noisy gates which are not detected by randomized benchmarking.

It is worth stressing that the gate analysis for the second set of results confirms the noise properties we previously found for the first set. In particular, the source of noise is mostly incoherent, since the unitarity decreases as the average gate infidelity increases in Fig. 6 (see inset in the lower plot). Moreover, the diamond distance is still of the order of  $10^{-1}$ , i.e., far away from the fault tolerant thresholds. Finally, the scaling of the state infidelity as a function of the channel length is again linear or sublinear.

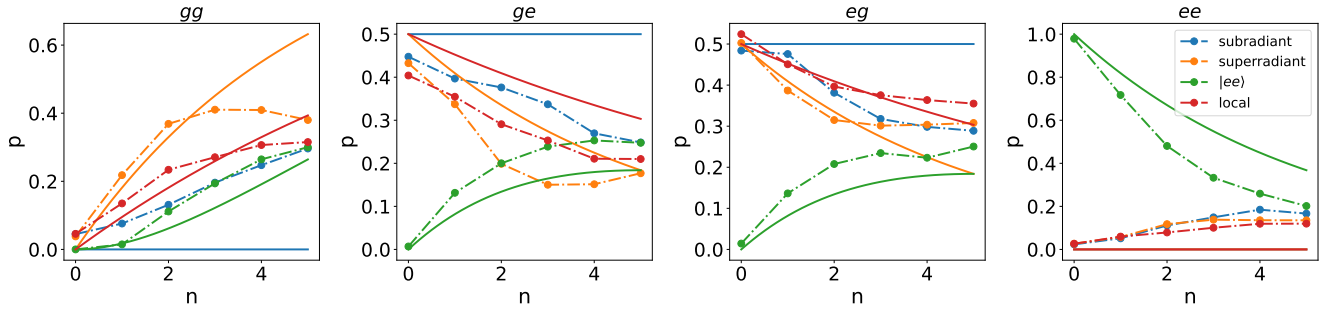


FIG. 5: Probability of finding the states  $|gg\rangle$ ,  $|ge\rangle$ ,  $|eg\rangle$ ,  $|ee\rangle$  (from left to right) through a projective measurement in the computational basis as a function of the number of steps in the MCM (second set of results), when the initial state is the superradiant state (blue), subradiant state (orange),  $|ee\rangle$  (green), and when the dynamics is local starting from the subradiant state (red). Solid lines: theoretical prediction based on the master equation. Markers of the dashed-dotted lines: experimental values. Some signatures of collective effects are still present, but they are mostly jeopardized by the presence of some very noisy gates. In particular, the subradiant state following a collective evolution (blue lines) is almost as fragile as with local dissipation only (red lines). The results have been obtained as averages over 37 realizations of the protocol, and the error bars are within the markers.

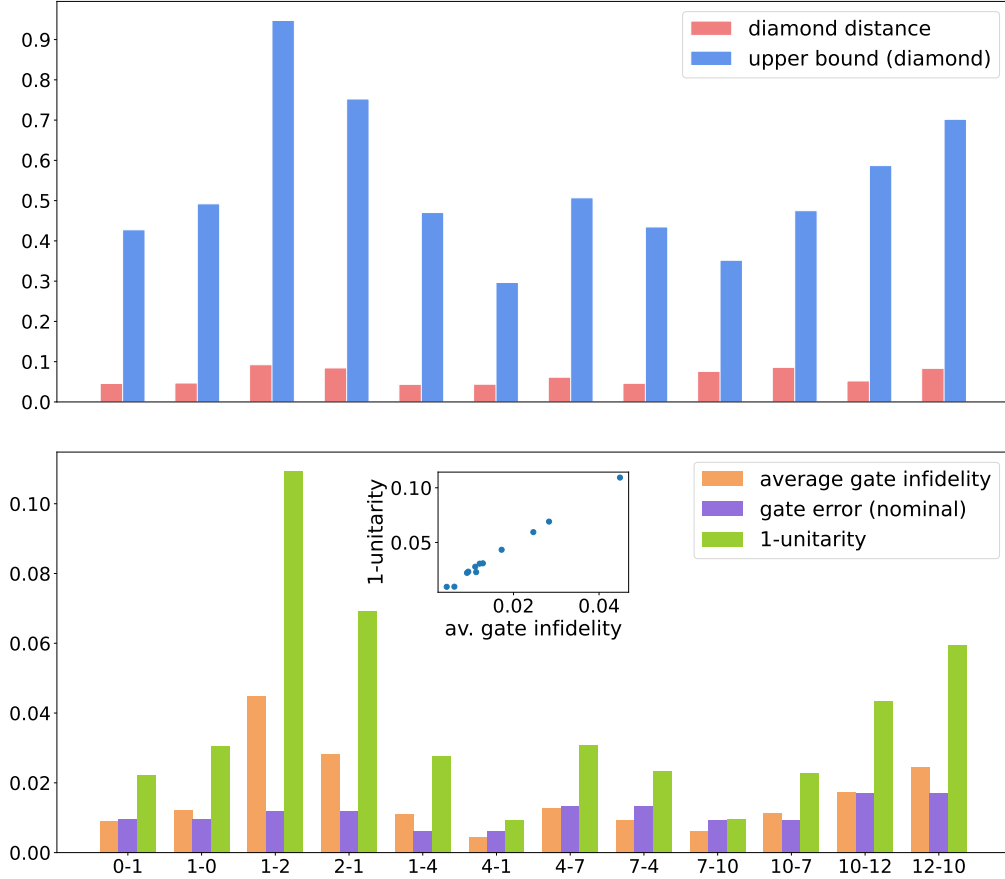


FIG. 6: Error analysis of the set of CNOT gates in `ibmq_guadalupe` employed for the simulation of the results in Fig. 5. The tick 0 – 1 on the x axis corresponds to the CNOT gate where “qubit 0” in `ibmq_guadalupe` is the control qubit and “qubit 1” is the target. Upper plot: diamond distance between ideal and noisy CNOT according to Eq. (4) (light red), and corresponding upper bound based on the average gate fidelity (light blue), as defined in Eq. (10). The CNOTs between qubit 1 and qubit 2 are clearly way noisier than according to their nominal gate error. Lower plot: experimental average gate fidelity  $\varphi(\mathcal{U}_g)$  introduced in Eq. (1) (orange), nominal average gate fidelity obtained through randomized benchmarking (purple) and  $1 - u(\mathcal{T})$  (green), where  $u(\mathcal{T})$  is the unitarity of the noisy gate, defined in Eq. (6). Inset: scatterplot with 1-unity vs average gate infidelity.

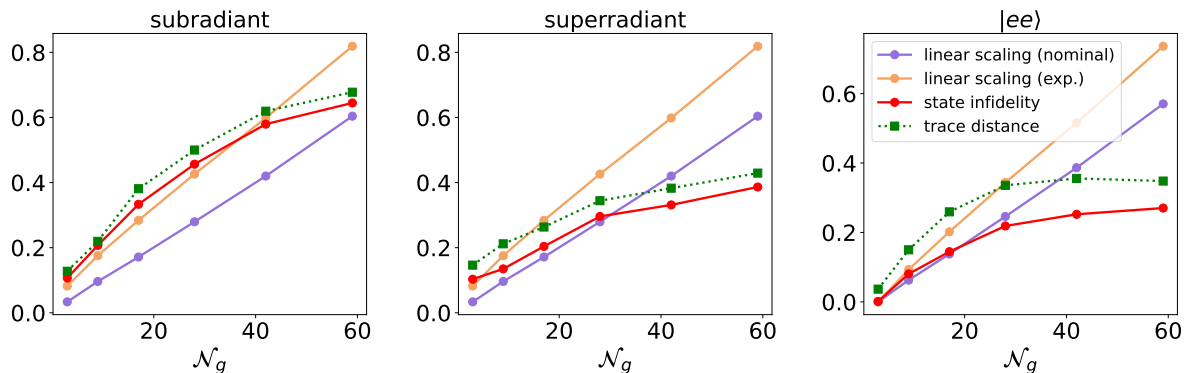


FIG. 7: Scaling of the error as a function of the number of gates in the algorithm  $\mathcal{N}_g$  during the simulation of the collective dynamics displayed in Fig. 5. The markers indicate the steps of the collision model. Solid orange and solid purple lines: linear scaling of respectively the experimental and the nominal average gate fidelity, given in Fig. 6.

Solid red line: experimental infidelity between the simulated state and the ideal one. Dotted green line: experimental trace distance between the simulated state and the ideal one. Both quantities display a linear or sublinear scaling as a function of  $\mathcal{N}_g$ .

## VI. CONCLUDING REMARKS AND PERSPECTIVES

We have presented the first fully quantum digital simulation of dissipative collective effects on a quantum computer. The state-of-the-art universal quantum computers do not allow for fault-tolerant computation yet, while they are subject to a considerable level of noise. However, we have shown that the algorithm we employed, namely the *multipartite collision model* (MCM) [31], simulates the superradiant and subradiant dynamics of two qubits colliding with a common ancilla with a good degree of accuracy (Fig. 2 and Fig. 10 in Appendix F).

In particular, we have simulated on a quantum computer the enhanced decay of the two-qubit state prepared in  $(|eg\rangle + |ge\rangle)/\sqrt{2}$ , which is a paradigmatic signature of superradiance, and the very slow decay of the state  $(|eg\rangle - |ge\rangle)/\sqrt{2}$ , which displays the emergence of subradiance. As a benchmark for these collective phenomena, we have also simulated the two-qubit dynamics in the presence of local decay only, and the results follow the theoretical scaling.

When dealing with current quantum devices, a rigorous theoretical and experimental analysis of the gate errors and the noise properties is essential. In Ref. [31], an error bound for the ideal multipartite collision model was derived using the  $1 \rightarrow 1$  superoperator norm. This error is essentially due to the inevitable choice of a small but finite algorithm timestep  $\Delta t$ , while the second-order Suzuki-Trotter decomposition of the MCM simulates the exact dynamics in the limit of infinitesimal timestep only.

In Sec. IV, we have presented a refined error bound that takes into account the possibility of employing noisy gates in the practical implementation of the MCM. Specifically, Proposition 1 generalizes the bound of Ref. [31] by making use of the diamond norm, which is a more precise norm for the distance between quantum

channels and, crucially, is employed in the estimation of a rigorous error threshold for quantum fault-tolerant computation. Moreover, Proposition 2 estimates an upper bound based on the diamond norm for the error we are incurring by using imperfect gates. While the quantum map associated with the MCM acts on the state of the system only, Proposition 2 expresses the error bound by taking into account the action of each gate on both the system and the ancillary qubits, and decomposes it into the sum of the individual errors of each quantum gate.

On the experimental side, the results on the noise analysis are depicted in Figs. 3 and 6. The full process tomography of all the CNOT gates employed in the algorithm has been crucial to understand the most important features of the noise on the platform. Starting from the results of the process tomography, we have indeed computed the average gate fidelity, the diamond norm and the unitarity of each gate, and compared them with the gate error provided by IBM, which is obtained through randomized benchmarking.

The conclusions we have drawn can be summarized in four points. First, the behavior of the unitarity as a function of the average gate fidelity indicates that the major source of error is dissipative, i.e., the “coherence of noise” [83] is low.

Second, the experimental average gate fidelity computed through full process tomography can sometimes differ from the randomized benchmarking value. This can also have repercussions for the outcome of the quantum simulation; e.g., the results in Fig. 5 are jeopardized by the action of some very noisy gates, the high infidelity of which is detected by process tomography but not by randomized benchmarking (see Fig. 6).

Third, the experimental diamond norm addresses the worst-case scenario, and therefore may be of little use for practical purposes. However, it is crucial for assessing the possibility for fault-tolerant quantum computation on a

given device, or for guaranteeing the efficient simulability of our algorithm. Our experimental results show that the gate error through the diamond norm is one or two orders of magnitude higher than the threshold values for fault-tolerant computation.

Fourth, the scaling of the infidelity between exact and simulated state as a function of the number of gates is linear or sublinear (see Figs. 4 and 7), i.e., much better than the worst-case scenario with quadratic scaling. This may be due to the fact that the major source of errors is dissipative and not coherent.

A crucial issue of open system simulation via interactions with ancillary qubits is the need for a new ancilla at each timestep. In this study, we have employed a train of ancillas that are swapped after each collision, so that a single ancillary qubit is finally interacting with the system qubits (see the discussion in Appendix E). A different solution consists in employing a reset gate to refresh the state of a single ancillary qubit at every timestep. However, our preliminary results based on the reset gate have shown a very quick emergence of decoherence (Fig. 11 in Appendix F). Reducing the gate time of the reset gate would therefore be a remarkable improvement for any simulation algorithm making use of ancillas. If this is not possible, enriching the topology of the near-term devices will crucially reduce the number of swap gates necessary to refresh the state of the ancilla for the  $n$ th collision. Yet another possibility for enhancing the accuracy of the quantum simulation would be working at the pulse level of the near-term devices [108]. This would basically correspond to performing an analog quantum simulation instead of a digital one, and has very recently led to improved results on the quantum simulation of many-body unitary systems [109].

To conclude, our experimental outcomes highlight how near-term quantum computers, even if far from being ideal, can already give useful and meaningful results on the simulation of collective quantum dynamics. Our findings are a proof-of-principle demonstration of the potential of the MCM algorithm for the exploration of topical and groundbreaking phenomena such as dissipative quantum phase transitions, quantum synchronization, and dissipative time crystals.

## ACKNOWLEDGMENTS

We acknowledge the use of IBM Quantum services for this work and the Quantum Technologies Platform QTEP (CSIC). The views expressed are those of the authors, and do not reflect the official policy or position of IBM or the IBM Quantum team. M.C., M.A.C.R., G.G.-P., and S.M. acknowledge financial support from the Academy of Finland via the Centre of Excellence program (Project No. 336810 and Project No. 336814). S.M. and G.G.-P. acknowledge support from the emmy.network foundation under the aegis of the Fondation de Luxembourg. G.G.-P. acknowledges

support from the Academy of Finland via the Postdoctoral Researcher program (Project no. 341985). M.C. and R.Z. acknowledge financial support from Centers and Units of Excellence in R&D (MDM-2017-0711) and from MICINN/AEI/FEDER and CAIB for projects PID2019-109094GB-C21/AEI/10.13039/501100011033 and PRD2018/47.

## Appendix A: Distances in quantum information

We will introduce here some distance measures for operators on the Hilbert space  $\mathcal{H}$  [41, 76, 81].

**Definition 5** (Schatten norms). The Schatten  $p$ -norm (with  $p \in [1, \infty]$ ) of an operator  $A \in \mathcal{B}(\mathcal{H})$  is defined as:

$$\|A\|_p = \text{Tr}[(\sqrt{A^\dagger A})^p]^{\frac{1}{p}}. \quad (\text{A1})$$

We will focus on the following two Schatten norms:

**Definition 6** (Trace norm). The trace norm (or 1-norm) of an operator  $A \in \mathcal{B}(\mathcal{H})$  is defined as:

$$\|A\|_1 = \text{Tr}[\sqrt{A^\dagger A}]. \quad (\text{A2})$$

**Definition 7** (Operator norm). The operator norm (or infinity norm) of an operator  $A \in \mathcal{B}(\mathcal{H})$  is the standard one in functional analysis, that is:

$$\|A\|_\infty = \max_{|v\rangle \in \mathcal{H}: \|v\|=1} \|A|v\rangle\|. \quad (\text{A3})$$

The vector norm (without any subscript)  $\|v\|$  is the standard Euclidean norm in the Hilbert space  $\mathcal{H}$ .

Here are some properties of the Schatten norms, in addition to the ones that define a norm, i.e., positivity, being zero only if  $A = 0$ , and fulfilling the triangle inequality  $\|A + B\|_p \leq \|A\|_p + \|B\|_p$ :

**Unitarily invariant:**  $\|UAV\|_p = \|A\|_p$  if  $U, V$  unitary.

**Sub-multiplicativity:**  $\|AB\|_p \leq \|A\|_p \|B\|_p$ .

**Monotonicity:**  $\|A\|_1 \geq \|A\|_p \geq \|A\|_q \geq \|A\|_\infty$  for  $p \leq q$ .

**Hölder's inequality:**  $\|AB\|_1 \leq \|A\|_p \|B\|_q$ , with  $p, q \in [1, \infty]$  (properly generalized) and  $1/p + 1/q = 1$ . In particular,  $\|AB\|_1 \leq \|A\|_1 \|B\|_\infty$ .

**Tensor product dependence:**  $\|A \otimes \mathbb{I}_B\|_p = (d_B)^{\frac{1}{p}} \|A\|_p$ . In particular,  $\|A \otimes \mathbb{I}_B\|_\infty = \|A\|_\infty$ ,  $\|A \otimes \mathbb{I}_B\|_1 = d_B \|A\|_1$ .

An additional useful figure of merit is the fidelity between two quantum states:

$$\mathcal{F}(\rho, \sigma) = \|\sqrt{\rho}\sqrt{\sigma}\|_1^2 = \left( \text{Tr}[\sqrt{\sqrt{\rho}\sigma\sqrt{\rho}}] \right)^2. \quad (\text{A4})$$

If  $\rho = |\psi\rangle\langle\psi|$  is pure, then  $\mathcal{F}(\rho, \sigma) = \text{Tr}[\rho\sigma]$ . The *infidelity*  $1 - \mathcal{F}(\rho, \sigma)$  is not a well-defined mathematical distance because it does not satisfy the triangle inequality.

## Appendix B: Steps of the multipartite collision model

We provide here the steps of the multipartite collision model introduced in Ref. [31] and discussed in Sec. III A. Let us consider the master equation Eq. (13) of a multipartite open system whose dynamics we aim to simulate. For simplicity, let us now assume that the subsystems  $1, \dots, M$  are qubits and the Lindblad operators in Eq. (14) are linear combinations of local operators acting on a single subsystem only. That is,  $L_k = \sum_{m=1}^M F_m^{(k)}$ , and each  $F_m^{(k)}$  is local on the  $m$ th subsystem. Then, the steps of the algorithm can be expressed as follows:

1. To each  $k = 1, \dots, J$  in Eq. (14) assign an ancillary qubit which will generate the corresponding term of the master equation.
2. For each  $k = 1, \dots, J$ , prepare the set of two-qubit quantum gates between the  $k$ th ancilla and the  $m$ th subsystem defined by:

$$U_k^{(m)}(t) = \exp[-ig_I t(\lambda_k F_m^{(k)} \sigma_k^+ + h.c.)], \quad (\text{B1})$$

where  $\lambda_k$  is a dimensionless parameter which is defined by  $\Gamma_k = |\lambda_k|^2$ , while the gate time  $t$  will eventually assume two values only, namely either  $\Delta t$  or  $\Delta t/2$ , where  $\Delta t$  is the timestep of the algorithm.  $g_I$  is a coupling constant which defines the collision strength, and in this paper it is fixed to  $g_I = \Delta t^{-1/2}$  [31].

3. Compose these quantum gates into a single unitary evolution  $U_k(\Delta t)$  as follows:

$$U_k(\Delta t) = \prod_{m=1}^M U_k^{(M-m+1)}(\Delta t/2) \prod_{m'=1}^M U_k^{(m')}(\Delta t/2). \quad (\text{B2})$$

Note that the two-qubit gate  $U_k^{(1)}(\Delta t)$  can be implemented as a single gate lasting for  $\Delta t$ , while all the other gates last for  $\Delta t/2$  and are executed twice during a single timestep. Eq. (B2) expresses the second-order Suzuki-Trotter decomposition of the interaction between the subsystems and the ancilla.

4. Follow the same procedure for each ancilla  $k = 1, \dots, J$ , and insert each gate sequence in a total unitary operator, where their order of execution does not matter:

$$U_I(\Delta t) = \prod_{k=1}^{d^{2M}-1} U_k(\Delta t). \quad (\text{B3})$$

5. Introduce a sequence of gates that simulate the effective Hamiltonian  $H_S$ , which is a free system Hamiltonian, during the timestep  $\Delta t$ :

$$U_{sim}(\Delta t) = U_S(\Delta t) \circ U_I(\Delta t), \quad (\text{B4})$$

with  $U_S(\Delta t) = \exp[-iH_S \Delta t]$ . Note that the latter step amounts to simulating the closed-system dynamics driven by the Hamiltonian  $H_S$ , which is a well-known task in quantum computing since the seminal paper by Lloyd [3].

6. Initialize the ancillary qubits in the ground state expressed by  $\rho_E = \bigotimes_{k=1}^J |0\rangle_k \langle 0|$ . Initialize the system qubits in the initial state of the open dynamics  $\rho_S(0)$ , as introduced in Eq. (12).
7. Implement a single timestep  $\Delta t$  of the algorithm by making the system and ancillary qubits evolve through the sequence of gates contained in the operator  $U_{sim}(\Delta t)$ . Then, to obtain the information on the state of the system only, trace out the degrees of freedom of the ancillas (the environment):

$$\phi_{\Delta t}[\rho_S] = \text{Tr}_E[U_{sim}(\Delta t)\rho_S \otimes \rho_E U_{sim}^\dagger(\Delta t)]. \quad (\text{B5})$$

$\phi_{\Delta t}$  is the quantum map associated with a single timestep of the multipartite collision model.

8. To implement  $n$  timesteps of the algorithm, apply the quantum map  $\phi_{\Delta t}$   $n$  times. That is, repeat the sequence of gates contained in  $U_{sim}(\Delta t)$  for  $n$  times using the same system qubits and a new set of fresh ancillas, initialized in the ground state  $\rho_E$ , for each timestep. The simulation of the dynamics until time  $t$  requires  $n = t/\Delta t$  repetitions, where the timestep of the algorithm  $\Delta t$  should be chosen as small as the experimental conditions allow for.

## Appendix C: Analytical solution of the dynamics

Here, we provide the analytical solution of the collective dynamics for the different initial states we consider in this work. Namely, we will obtain  $\rho_S(t) = \exp \mathcal{L}t[\rho_S(0)]$ , where  $\mathcal{L}$  is given by Eq. (19), and for  $\rho_S(0) = \rho_{\text{sup}}, \rho_{\text{sub}}$  and  $\rho_{ee} = |ee\rangle \langle ee|$ , which have been introduced in Sec. III B. We will also find the evolution of  $\rho_{\text{sub}}$  when the dissipator is local and incoherent, that is, in the absence of the decoherence-free subspace.

A straightforward calculation yields  $\mathcal{L}[\rho_{\text{sub}}] = 0$ , therefore

$$\exp \mathcal{L}t[\rho_{\text{sub}}] = \rho_{\text{sub}}, \quad (\text{C1})$$

i.e.,  $\rho_{\text{sub}}$  is a steady state of the dynamics and lives in a decoherence-free subspace.

As for the superradiant state, we observe:

$$\mathcal{L}[\rho_{\text{sup}}] = -2\gamma(\rho_{\text{sup}} - \rho_{gg}), \quad \mathcal{L}[\rho_{gg}] = 0, \quad (\text{C2})$$

where  $\rho_{gg} = |gg\rangle \langle gg|$  is the ground state, which is stationary because the master equation (19) is at zero temperature. Therefore, the operator  $\rho_{\text{sup}} - \rho_{gg}$  is an eigenvector of the Liouvillian with eigenvalue  $-2\gamma$ . We finally



obtain:

$$\begin{aligned} \exp \mathcal{L}t[\rho_{\text{sup}}] &= \exp \mathcal{L}t[\rho_{\text{sup}} - \rho_{gg}] + \rho_{gg} \\ &= e^{-2\gamma t} \rho_{\text{sup}} + (1 - e^{-2\gamma t}) \rho_{gg}. \end{aligned} \quad (\text{C3})$$

Using the above result, we immediately find the formula for the intensity of the superradiant emission in Eq. (21).

Computing the evolution of  $\rho_{ee}$  is slightly more involved. First of all, we calculate:

$$\mathcal{L}[\rho_{ee}] = 2\gamma(\rho_{\text{sup}} - \rho_{ee}). \quad (\text{C4})$$

Then, we can merge the results of the above equation and Eq. (C2) into a single system of linear differential equations written as:

$$\frac{d}{dt} \mathbf{v}(t) = M \mathbf{v}(t), \quad (\text{C5})$$

where  $\mathbf{v}(t) = (\exp \mathcal{L}t[\rho_{gg}], \exp \mathcal{L}t[\rho_{\text{sup}}], \exp \mathcal{L}t[\rho_{ee}])^T$ ,

$$M = \gamma \begin{pmatrix} 0 & 0 & 0 \\ 2 & -2 & 0 \\ 0 & 2 & -2 \end{pmatrix}. \quad (\text{C6})$$

One way to tackle this problem is to solve each differential equation starting from the trivial one for the steady state, and then to insert this solution into the following equation, which will now be independent and affine, and so on. Another instructive (and more general) way to find the solution of the dynamics is to compute  $\mathbf{v}(t) = \exp(Mt) \mathbf{v}(0)$  by getting the Jordan–Chevalley decomposition of  $M$  [110]. Indeed,  $M$  has the eigenvalue 0 with eigenvector  $(1, 1, 1)^T$ , and the eigenvalue  $-2$  with multiplicity 2 and a one-dimensional eigenspace spanned by  $(0, 0, 1)^T$ . That is,  $M$  is not diagonalizable. So, we need to obtain its Jordan decomposition as  $M = PJ_M P^{-1}$ , with:

$$J_M = \gamma \begin{pmatrix} 0 & 0 & 0 \\ 0 & -2 & 1 \\ 0 & 0 & -2 \end{pmatrix}, \quad P = \begin{pmatrix} 1 & 0 & 0 \\ 1 & 0 & 1 \\ 1 & 2 & 0 \end{pmatrix}. \quad (\text{C7})$$

Then, the Jordan-Chevalley decomposition is trivially expressed by  $J_M = D_M + N_M$ , where  $D_M$  is the diagonal matrix with the same elements of  $J_M$  on the diagonal, while  $N_M$  is a matrix whose only non-zero element is the off-diagonal 1 in  $J_M$ .  $N_M$  is nilpotent ( $N_M^2 = 0$ ), and  $[N_M, D_M] = 0$ . Then, after some simple matrix algebra we find

$$\begin{aligned} e^{Mt} &= e^{PJ_M P^{-1}t} = P e^{D_M t} e^{N_M t} P^{-1} \\ &= \begin{pmatrix} 1 & 0 & 0 \\ 1 - e^{-2\gamma t} & e^{-2\gamma t} & 0 \\ 1 - e^{-2\gamma t}(1 + 2\gamma t) & 2\gamma t e^{-2\gamma t} & e^{-2\gamma t} \end{pmatrix}. \end{aligned} \quad (\text{C8})$$

Finally, we obtain the evolution of  $\rho_{ee}$ :

$$\begin{aligned} \exp \mathcal{L}t[\rho_{ee}] &= e^{-2\gamma t} \rho_{ee} + 2\gamma t e^{-2\gamma t} \rho_{\text{sup}} \\ &\quad + (1 - e^{-2\gamma t}(1 + 2\gamma t)) \rho_{gg}. \end{aligned} \quad (\text{C9})$$

Once again, the enhanced decay rate  $2\gamma$  is a signature of collective effects in the dynamics.

Let us now compute the local incoherent evolution of  $\rho_{\text{sub}}$ . The Liouvillian driving this type of dynamics is:

$$\mathcal{L}_{\text{loc}}[\rho_S] = \sum_{j=1,2} \gamma \left( \sigma_j^- \rho_S \sigma_j^+ - \frac{1}{2} \{ \sigma_j^+ \sigma_j^-, \rho_S \} \right), \quad (\text{C10})$$

where, for simplicity, we have taken the same decay rate  $\gamma$  for both qubits. Straightforwardly,  $\mathcal{L}_{\text{loc}}[\rho_{\text{sub}}] = \gamma(\rho_{gg} - \rho_{\text{sub}})$ , therefore

$$\exp \mathcal{L}_{\text{loc}}t[\rho_{\text{sub}}] = e^{-\gamma t} \rho_{\text{sub}} + (1 - e^{-\gamma t}) \rho_{gg}. \quad (\text{C11})$$

As expected, the subradiant state decays toward the ground with the standard incoherent rate  $\gamma$ .

## Appendix D: Proofs of the results in Sec. IV

### 1. Diamond distance $\epsilon_s^\diamond$ for the ideal case

We want to prove the bound

$$\|\phi_{\Delta t} - \exp \mathcal{L}\Delta t\|_\diamond \leq \mathcal{B}_{1 \rightarrow 1}. \quad (\text{D1})$$

To check its validity, note that the bounds we need to estimate are, according to the Supplemental Material (SM) of Ref. [31],

$$\|\mathcal{L}\|_\diamond, \quad \|\mathcal{R}_c(\text{Tr}_E[U(\Delta t) \cdot \otimes \rho_E U^\dagger(\Delta t)])\|_\diamond, \quad (\text{D2})$$

where  $\mathcal{R}_c$  is a remainder of the expansion of the MCM unitaries (see the original paper [31] for details). For our purposes, it is sufficient to assume that it is a polynomial function of operators.

Let us first show that the bound on the  $1 \rightarrow 1$  norm of the Liouvillian found is valid also for the diamond norm. This result is also stated in Ref. [111] (SM). The crucial point is that, despite the  $1 \rightarrow 1$  having the undesirable property of not scaling well in the presence of a tensor product, by means of the Hölder's inequality introduced in Sec. II, the error bound can be written as a function of infinity norms only, which are stable. Therefore, estimating the same bound with the diamond norm leads to the same equations. Let us show this.

In the following,  $\mathbb{I}_A$  will be the identity operator on a copy of the space of the bounded operators on the Hilbert space of the system  $\mathcal{B}(\mathcal{H})$ , according to the definition of the diamond norm in Eq. (3). We evaluate:

$$\begin{aligned} \|\mathcal{L} \otimes \mathbb{I}_A[\rho]\|_1 &= -i \|[H \otimes \mathbb{I}_A, \rho]\|_1 \\ &\quad + \sum_k \left( \left\| L_k \otimes \mathbb{I}_A \rho L_k^\dagger \otimes \mathbb{I}_A - \frac{1}{2} \{L_k^\dagger L_k \otimes \mathbb{I}_A\} \right\|_1 \right) \\ &\leq 2(\|H\|_\infty + \sum_k \|L_k\|_\infty^2), \end{aligned} \quad (\text{D3})$$

under the assumption that  $\|\rho\|_1 = 1$ . We have used the Hölder's inequality and the multiplicativity of the infinity norm. The above bound is the same as for the  $1 \rightarrow 1$  norm. Indeed, evaluating everything on a basis of the extended Hilbert space we observe:

$$\mathcal{L} \otimes \mathbb{I}_A[|\psi_j \psi_k\rangle \langle \psi_l \psi_m|] = \mathcal{L}[|\psi_j\rangle \langle \psi_l|] \otimes |\psi_k\rangle \langle \psi_m|, \quad (\text{D4})$$

and we can write  $\rho$  as

$$\rho = \sum_{j,k,l,m} a_{jklm} |\psi_j \psi_k\rangle \langle \psi_l \psi_m|. \quad (\text{D5})$$

Therefore,

$$\begin{aligned} \mathcal{L} \otimes \mathbb{I}_A[\rho] &= \sum_{j,k,l,m} a_{jklm} (-i[H, |\psi_j\rangle \langle \psi_l|] \otimes |\psi_k\rangle \langle \psi_m| \\ &\quad + \sum_k (L_k |\psi_j\rangle \langle \psi_l| L_k^\dagger - \dots) \otimes |\psi_k\rangle \langle \psi_m|), \end{aligned} \quad (\text{D6})$$

showing that Eq. (D3) is correct. This is basically due to the linearity of quantum channels.

Equivalently, for the remainder:

$$\begin{aligned} &\sum_{j,k,l,m} a_{jklm} \text{Tr}_E[U(\Delta t) |\psi_j\rangle \langle \psi_l| \otimes \rho_E U^\dagger(\Delta t)] \otimes |\psi_k\rangle \langle \psi_m| \\ &= \sum_{j,k,l,m} a_{jklm} \text{Tr}_E[U(\Delta t) \otimes \mathbb{I}_A |\psi_j \psi_k\rangle \langle \psi_l \psi_m| \otimes \rho_E U^\dagger(\Delta t) \otimes \mathbb{I}_A] = \text{Tr}_E[U(\Delta t) \otimes \mathbb{I}_A \rho \otimes \rho_E U^\dagger(\Delta t) \otimes \mathbb{I}_A]. \end{aligned} \quad (\text{D7})$$

Therefore, when evaluating the trace norm of the above expression, we can still find a bound which only depends on  $\|U(\Delta t) \otimes \mathbb{I}_A\|_\infty$ , that is, on  $\|U(\Delta t)\|_\infty$ . This is the same bound found in Ref. [31], expressed in Eq. (18) of the main text.

## 2. Diamond distance $\epsilon_m^*$ between ideal and noisy MCM map

The estimation of an upper bound for  $\epsilon_m^*$  can be performed as follows:

$$\begin{aligned} \|\phi_{\Delta t}^* - \phi_{\Delta t}\|_\diamond &= \left\| \text{Tr}_E \left[ \prod_j \mathcal{E}_j \prod_i \mathbb{I}_S \otimes \mathcal{G}_i [\cdot \otimes \rho_E] \right] - \text{Tr}_E \left[ \prod_j \mathcal{U}_j [\cdot \otimes \rho_E] \right] \right\|_\diamond \\ &= \left\| \text{Tr}_E \left[ \left( \prod_j \mathcal{E}_j \prod_i \mathbb{I}_S \otimes \mathcal{G}_i - \prod_j \mathcal{U}_j \prod_i \mathbb{I}_{SE} \right) [\cdot \otimes \rho_E] \right] \right\|_\diamond \\ &= \sup_{\rho_{SA}: \|\rho_{SA}\|_1=1} \left\| \text{Tr}_E \left[ \left( \prod_j \mathcal{E}_j \prod_i \mathbb{I}_S \otimes \mathcal{G}_i - \prod_j \mathcal{U}_j \prod_i \mathbb{I}_{SE} \right) \otimes \mathbb{I}_A [\rho_{SA} \otimes \rho_E] \right] \right\|_1 \\ &\leq \sup_{\rho_{SA}: \|\rho_{SA}\|_1=1} \left\| \left( \prod_j \mathcal{E}_j \prod_i \mathbb{I}_S \otimes \mathcal{G}_i - \prod_j \mathcal{U}_j \prod_i \mathbb{I}_{SE} \right) \otimes \mathbb{I}_A [\rho_{SA} \otimes \rho_E] \right\|_1 \\ &\leq \sup_{\rho_{SA} \otimes \rho_E: \|\rho_{SA}\|_1=1, \|\rho_E\|=1} \left\| \left( \prod_j \mathcal{E}_j \prod_i \mathbb{I}_S \otimes \mathcal{G}_i - \prod_j \mathcal{U}_j \prod_i \mathbb{I}_{SE} \right) \otimes \mathbb{I}_A [\rho_{SA} \otimes \rho_E] \right\|_1 \\ &\leq \sup_{\rho_{SAE}: \|\rho_{SAE}\|_1=1} \left\| \left( \prod_j \mathcal{E}_j \prod_i \mathbb{I}_S \otimes \mathcal{G}_i - \prod_j \mathcal{U}_j \prod_i \mathbb{I}_{SE} \right) \otimes \mathbb{I}_A [\rho_{SAE}] \right\|_1 \\ &= \left\| \prod_j \mathcal{E}_j \prod_i \mathbb{I}_S \otimes \mathcal{G}_i - \prod_j \mathcal{U}_j \prod_i \mathbb{I}_{SE} \right\|_\diamond \leq \sum_j \|\mathcal{E}_j - \mathcal{U}_j\|_\diamond + \sum_i \|\mathcal{G}_i - \mathbb{I}_E\|_\diamond. \end{aligned} \quad (\text{D8})$$

Note that we are employing the subscript “ $A$ ” to denote states and operators that belong or act on a copy of the Hilbert space of the system, according to the definition of the diamond norm in Eq. (3). In contrast, the subscripts “ $S$ ” and “ $E$ ” indicate respectively the “original” Hilbert space of the system and the Hilbert space of the ancillary qubits. To obtain the final result in Eq. (D8), we have employed the fact that  $\|\text{Tr}_E[O]\|_1 \leq \|O\|_1$  [112] and the sub-multiplicativity of the diamond norm, as in Eq. (5).

Finally, note that the diamond distance between the map  $\mathcal{G}_i$  and the identity does not assume that the ancilla is ideally initialized in the ground state. So, Eq. (D8) is valid also for scenarios with different choices of initial states. Moreover, if the quantum channel describing the noise for the state preparation on the backend is not known, one may tighten the bound by minimizing  $\|\mathcal{G}_i - \mathbb{I}_E\|_\diamond$  over all the channels  $\mathcal{G}_i$  that map the ideal initial state of the ancilla into the observed noisy state.

## Appendix E: Experimental scheme and methods

### 1. Topology of the backend

The IBM quantum computers are often recalibrated to optimize their performance. That is, their qubit and gate parameters are often modified at the level of the hardware. As a consequence, the gate and readout errors change after every calibration. For our purposes, we want to run the above-listed protocols with a fixed set of experimental parameters. So, we need to employ a near-term device with a sufficient time interval between two calibration procedures (running all the necessary protocols listed in Sec. V takes roughly 3 hours). The 16-qubits backend `ibmq_guadalupe` is very stable in this sense (it is usually re-calibrated once per day), and so we have chosen it for running our algorithm.

When we write the (Qiskit) code to run a quantum algorithm on a near-term device, we must always take into account the topology of the latter, because it constraints the operations we can actually perform on the platform: only CNOTs between nearby qubits can be directly implemented. The topology of `ibmq_guadalupe` is depicted in Fig. 8.

For the experiments presented in Sec. V, we have used the following sets of qubits on `ibmq_guadalupe`: the system qubits are (0, 2). The ancillary qubits for the collective dynamics are (1, 4, 7, 10, 12). We have employed the same set of ancillary qubits for the local dissipative dynamics on the system qubit 0, while the ancillas for the local decay of the system qubit 2 are (3, 5, 8, 11, 14).

Note that the ancillary qubit 1 (and 3 for the local decay of the system qubit 2) is the only one that is directly linked to both the system qubits. So, we are only allowed to implement the CNOTs 0-1, 1-0, 1-2 and 2-1 to evolve the state of the system. To make the system qubits interact with the remaining ancillas, we need to swap the states of the ancillary qubit 1 with the one of the ancil-

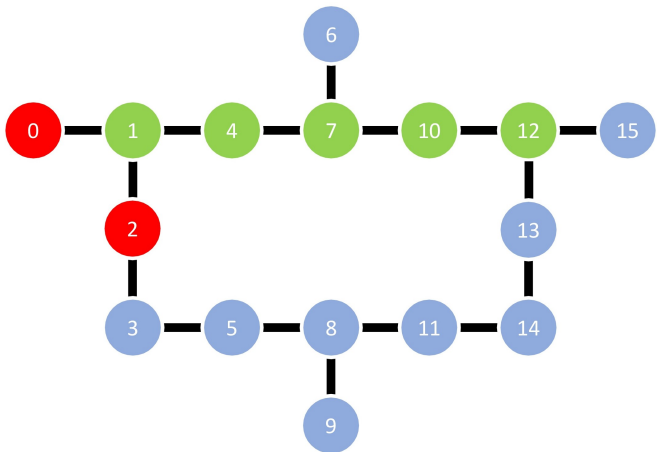


FIG. 8: Topology of `ibmq_guadalupe` with 16 qubits.

The links denote the possibility of implementing a direct two-qubit gate between a pair of qubits. The red (green) qubits are employed as system (ancillary) qubits in the simulation of dissipative collective effects.

lary qubit 4, then 4 with 7 and again 1 with 4, then 7 with 10, and so on. This requires an additional number of CNOT gates (three per each swap) that increases at each timestep. Indeed, given a train of ancillary qubits from 1 (which is directly linked to the system qubits) to  $n$ , we need exactly  $n-1$  swaps to make the  $n$ -th ancilla interact with the system. This is a well-known issue of near-term devices with limited connectivity [35]. In the next subsection, we will show how we have been able to optimize the number of necessary gates by employing, under certain circumstances, two CNOTs only to perform a single swap.

Possible ways to tackle this problem in the near future may be: i) Adding more qubit-qubit links to the topology of the backend, so as to reduce the number of swaps necessary to connect a distant ancilla with the system qubits; ii) Implementing a fast and efficient reset gate to be applied on the closest ancillary qubit (qubit 1 in Fig. 8) at every timestep. In fact, by employing a reset gate, we would need a single ancillary qubit only to be re-initialized on the ground state after each collision, or equivalently, thinking of more complex physical problems, one ancillary qubit for each Lindblad operator in the dissipator in Eq. (14) [31], according to the discussion in Sec. III. The reset gate is already available on `ibmq_guadalupe`. However, it is a very slow gate and decoherence rapidly emerges after a couple of applications thereof, as we will show in Appendix F. Therefore, improvements on the reset gate time would be extremely beneficial for the quantum simulation of open systems via MCM.

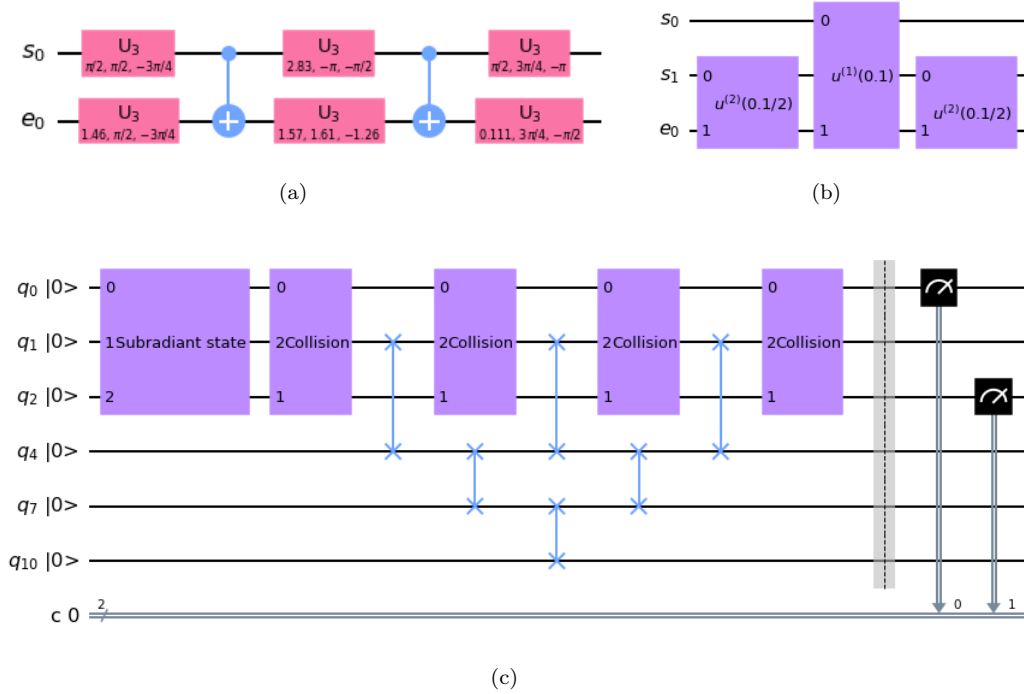


FIG. 9: (a): Decomposition of the gate  $U^{(1)}(0.1)$  defined in Eq. (23) on the IBM quantum computer, applied on a system qubit  $s_0$  and an ancillary qubit  $e_0$ . The gates  $U_3$  are single-qubit rotations defined by the three Euler angles given in the figure, and are elementary gates available on the IBM quantum computers [65]. Two CNOT gates are also necessary to implement the system-ancilla interaction. (b): Scheme of a single collision of the MCM with  $\Delta t = 0.1$  on the IBM quantum computer. The gates  $U^{(1)}(0.1)$  and  $U^{(2)}(0.1/2)$  are defined in Eq. (23), and their decomposition into elementary gates is given in subfigure (a). (c): Experimental circuit scheme to implement four collisions of the MCM on `ibmq_guadalupe`, starting from the subradiant state. All the qubits are initialized in the ground state, and the system qubits are then prepared in the subradiant state using the environment qubit 1 as an ancilla (there is no direct interaction between them). After each collision, as given by the decomposition in subfigure (b), a new fresh state of the ancillary qubit 1 is prepared by swapping the latter with the remaining ancillas of the train.

## 2. Algorithm implementation and optimization

The circuit scheme to implement the algorithm discussed in Sec. III B on `ibmq_guadalupe` is shown in Fig. 9. The unitary interaction between a single system qubit and the ancilla, i.e., Eq. (B1) of the MCM, or equivalently  $U^{(i)}(\Delta t)$  in Eq. (23) for the simulation of super- and sub-radiance, is depicted in Fig. 9(a). To implement it on the hardware, two CNOT gates and some single-qubit rotations are required. Since the gate error of single-qubit rotations is one or two orders of magnitude lower than the CNOT error [65] (typically, the infidelity of 1-qubit gates is of the order of  $10^{-4}$ ), the CNOTs in the circuit bring the largest contribution to the overall error of the algorithm.

Fig. 9(b) represents a single collision between the system qubits and the ancilla, which is composed of the three applications of the gates described in Fig. 9(a), according to the second-order Suzuki-Trotter decomposition of the

MCM in Eq. (B2). Finally, Fig. 9(c) shows the implementation of the algorithm on `ibmq_guadalupe`, starting from the subradiant state and up to  $n = 4$  collisions. The preparation of the subradiant and superradiant states requires one CNOT and some single-qubit gates [41, 65]. In addition, due to the topology of the backend in Fig. 8, there is no direct link between the system qubits 0 and 2. Therefore, we need to employ the ancillary qubit 1 to prepare a Bell state between qubits 0 and 2. We then swap the state of the qubit 1 with the one of qubit 2. In contrast, the preparation of  $|ee\rangle$  only needs two local  $X$  gates, and is therefore way less noisy.

As shown in Fig. 9(c), after the state preparation we are ready to implement a single timestep of the MCM by applying the routine in Fig. 9(b) to the system qubits and the ancilla. To simulate further collisions, we need to re-initialize the state of the ancillary qubit 1 by swapping it with the fresh ancillas in the train (4,7,10,12). We finally measure the state of the system qubits to reconstruct the statistics of the outcomes after the  $n$ th collision.

The state preparation, the interactions for every timestep and the swaps in the train of ancillas require a large number of noisy CNOT gates. However, we can optimize this number by noticing that, if  $C_{01}$  is the CNOT with qubit 0 as control and qubit 1 as target, while  $S_{01}$  is the swap gate between these qubits, then  $S_{01}|0\rangle \otimes |\psi\rangle = C_{01}C_{10}|0\rangle \otimes |\psi\rangle$ . That is, we need two CNOTs only to implement the swap gate if one of the qubits starts in the ground state. Ideally, all the swap gates in the algorithm act at least on one qubit in the ground state. However, we have verified that the 2-CNOT swap is reliable only when the qubit in  $|0\rangle$  is a fresh ancilla that has not been manipulated before. Otherwise, the error coming from the fact that this qubit is not exactly in  $|0\rangle$  (due to noise and imperfections in the algorithm implementation) jeopardizes the advantage of using one CNOT less. As a consequence, we can remove only 5 CNOT gates from the actual protocol (one for each ancillary qubit). Finally, note that employing a reset gate would drastically reduce the number of two-qubit gates in the algorithm. Indeed, the train of ancillas at the  $n$ th collision requires  $(n-1) \times (3n-1)$  CNOTs.

### 3. Methods to estimate the figures of merit

The outcome probabilities displayed in Figs. 2 and 5 have been obtained through standard projective measurements in the computational basis, which are available on the IBM quantum computer, as in the circuit scheme of Fig. 9(c). The results have been computed as averages over 37 realizations of the protocol, and each realization had 8192 shots (i.e., repetitions of the algorithm). We have found that the standard deviation over the 37 realizations always leads to small error bars that are within the markers shown in the plots.

The process tomography of the state after each collision (Figs. 4 and 7) and of the CNOT gates (Figs. 3 and 6) has been computed by running the process tomography circuits on the backend, which are available on `qiskit.ignis` [65]. Then, the results have been fitted to reconstruct the Choi matrix of the process, through the Qiskit class `ProcessTomographyFitter`.

The trace distance and the fidelity between ideal and simulated state at each timestep have been computed through the in-built functions in Qiskit and Qutip [113]. Starting from the Choi matrix of the ideal and simulated gate, the diamond distance and the average gate fidelity can be evaluated through the Qiskit functions `average_gate_fidelity` and `diamond_norm`. In particular, the latter makes use of the semidefinite program developed in Ref. [80]. Finally, we have computed the unitarity of each gate by employing both definitions in Eqs. (6) and (7). In particular, we have introduced two new functions in Qiskit to obtain these values starting from the Choi matrix of the process. We have checked that the values computed according to each definition coincide.

Readout error mitigation has been performed for all the results shown in the paper. The calibration filters have been obtained through the class `CompleteMeasFitter` and the function `complete_meas_cal` in Qiskit.

## Appendix F: Further results

### 1. Subradiant dynamics on `ibmq_toronto`

The validity of the experimental results presented in Sec. V is not restricted to `ibmq_guadalupe`, or to a specific choice of system and ancillary qubits. Indeed, in Fig. 10 we show the experimental outcomes for the MCM implemented on `ibmq_toronto`, which is a different IBM backend with 27 qubits. We have run the MCM to simulate the collective subradiant dynamics starting from different pairs of system qubits, each of which was connected to a suitable train of ancillas. The findings plotted in Fig. 10 confirm the emergence of collective effects in the quantum simulation, as discussed in Sec. V and Fig. 2. Once again, the gate errors break the decoherence-free subspace of the ideal dynamics, but still, comparing Fig. 10 with Fig. 2, we observe a slower decay of the subradiant state than in the scenario with local dissipation only. In some cases, as for the system pair (9,11) (we refer the reader to the Qiskit documentation for the topology of the backends [65]), the subradiance on `ibmq_toronto` is actually enhanced with respect to the best results obtained on `ibmq_guadalupe`.

Due to the fact that `ibmq_toronto` is re-calibrated much more often than `ibmq_guadalupe`, it has not been possible to perform the process tomographies necessary for the gate analysis we introduced in Sec. V. However, the crucial readout error mitigation has been correctly applied to the results in Fig. 10.

### 2. Refreshing the ancilla through the reset gate

As discussed in Appendix E, a possible way to optimize the necessary resources for the quantum simulation of the MCM is represented by the reset gate available on some IBM computers [65], which re-initializes the state of the target qubit in the ground state  $|0\rangle$ . With a reset gate at our disposal, we need a single ancillary qubit (two ancillary qubits in the case of the local decay) to simulate collective effects, since we can re-initialize it after each collision and avoid using a whole train of ancillas, which must be swapped. It goes without saying that this would represent a huge improvement in the number of necessary qubits and gates.

We have run a protocol based on the MCM with the reset gate on `ibmq_guadalupe`, and the results are shown in Fig. 11. The possibility of using always the same ancilla allows us to implement more collisions (here, we have chosen  $n = 10$ ). However, the accuracy of the simulation

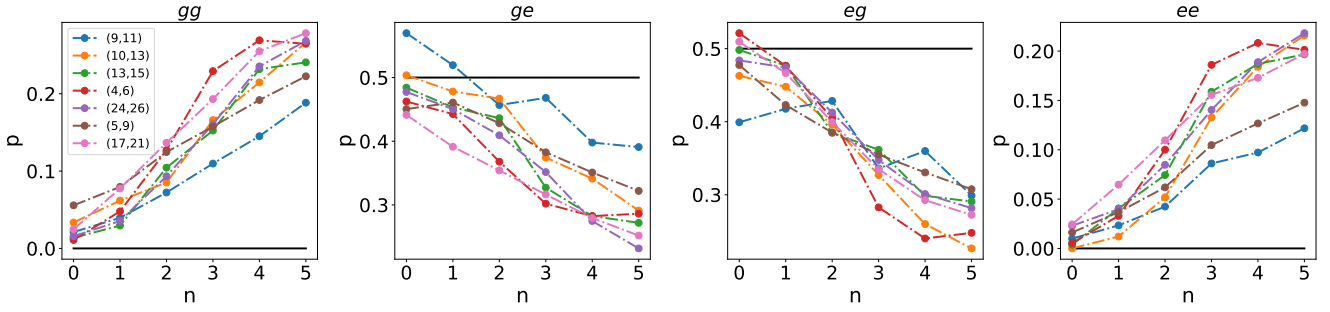


FIG. 10: Probability of finding the states  $|gg\rangle$ ,  $|ge\rangle$ ,  $|eg\rangle$ ,  $|ee\rangle$  (from left to right) through a projective measurement in the computational basis as a function of the number of steps in the MCM on `ibmq_toronto`, when the initial state is the subradiant state. Solid black lines: theoretical prediction based on the master equation. Markers of the dashed-dotted lines: experimental values. Different colors denote different initial pairs of system qubits in the topology of `ibmq_toronto`, each of which interacts with a corresponding train of ancillas.

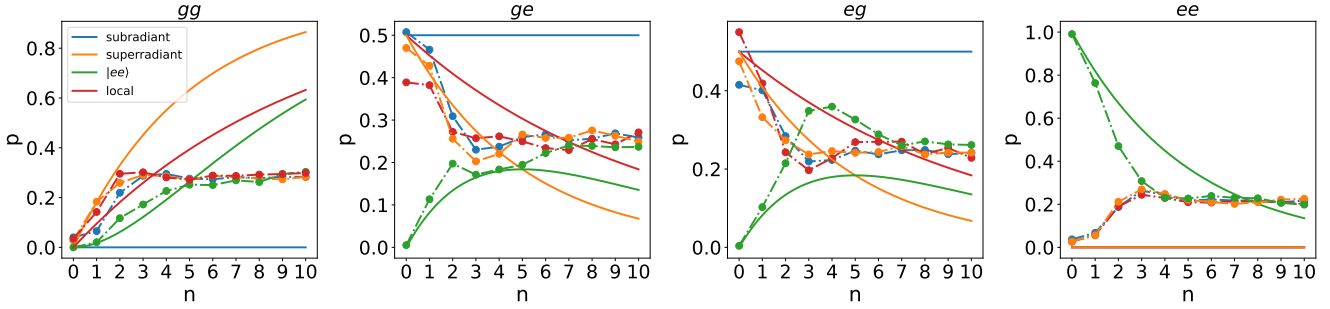


FIG. 11: Probability of finding the states  $|gg\rangle$ ,  $|ge\rangle$ ,  $|eg\rangle$ ,  $|ee\rangle$  (from left to right) through a projective measurement in the computational basis as a function of the number of steps in the MCM on `ibmq_guadalupe`, when the initial state is the superradiant state (blue), subradiant state (orange),  $|ee\rangle$  (green), and when the dynamics is local starting from the subradiant state (red). Solid lines: theoretical prediction based on the master equation. Markers of the dashed-dotted lines: experimental values. The reset gate is employed to refresh the state of the ancillary qubit after each timestep.

is clearly much worse than for the MCM via trains of ancillas. Indeed, after one or two collisions, decoherence arises and the state of the system qubits reaches what looks like a thermal stationary state with no coherences at all.

This is due to the fact that the running time of the reset gate is much longer than the one of standard single- and two-qubit gates [65]. That is, implementing a dissipative channel on the quantum platform takes more time than

performing coherent operations. Therefore, employing the reset gate even just a couple of times is enough for decoherence to occur.

In conclusion, at present (the results in Fig. 11 have been obtained during December 2021), the reset gate is not a feasible solution to reduce the number of necessary resources for the quantum simulation of the MCM. Similar results have been obtained on different IBM computers, including `ibmq_toronto` and `ibmq_mumbai`.

- 
- [1] R. P. Feynman, Simulating physics with computers, *Int. J. Theor. Phys.* **21**, 467 (1982).
  - [2] E. Altman *et al.*, Quantum Simulators: Architectures and Opportunities, *PRX Quantum* **2**, 017003 (2021).
  - [3] S. Lloyd, Universal Quantum Simulators, *Science*. **273**, 1073 (1996).
  - [4] I. M. Georgescu, S. Ashhab, and F. Nori, Quantum simulation, *Rev. Mod. Phys.* **86**, 153 (2014).
  - [5] A. A. Houck, H. E. Türeci, and J. Koch, On-chip quantum simulation with superconducting circuits, *Nat. Phys.* **8**, 292 (2012).
  - [6] G. S. Paraoanu, Recent Progress in Quantum Simulation Using Superconducting Circuits, *J. Low Temp. Phys.* **175**, 633 (2014).
  - [7] M. Kjaergaard, M. E. Schwartz, J. Braumüller, P. Krantz, J. I. Wang, S. Gustavsson, and W. D. Oliver, Superconducting Qubits: Current State of Play, *Annu. Rev. Condens. Matter Phys.* **11**, 369 (2020).
  - [8] A. Blais, A. L. Grimsmo, S. M. Girvin, and A. Wallraff, Circuit quantum electrodynamics, *Rev. Mod. Phys.* **93**,

- 025005 (2021).
- [9] R. Blatt and C. F. Roos, Quantum simulations with trapped ions, *Nat. Phys.* **8**, 277 (2012).
- [10] J. Zhang, G. Pagano, P. W. Hess, A. Kyprianidis, P. Becker, H. Kaplan, A. V. Gorshkov, Z.-X. Gong, and C. Monroe, Observation of a many-body dynamical phase transition with a 53-qubit quantum simulator, *Nature* **551**, 601 (2017).
- [11] C. Monroe, W. C. Campbell, L.-M. Duan, Z.-X. Gong, A. V. Gorshkov, P. W. Hess, R. Islam, K. Kim, N. M. Linke, G. Pagano, P. Richerme, C. Senko, and N. Y. Yao, Programmable quantum simulations of spin systems with trapped ions, *Rev. Mod. Phys.* **93**, 025001 (2021).
- [12] A. Aspuru-Guzik and P. Walther, Photonic quantum simulators, *Nat. Phys.* **8**, 285 (2012).
- [13] I. Bloch, J. Dalibard, and S. Nascimbène, Quantum simulations with ultracold quantum gases, *Nat. Phys.* **8**, 267 (2012).
- [14] C. Gross and I. Bloch, Quantum simulations with ultracold atoms in optical lattices, *Science*. **357**, 995 (2017).
- [15] H.-P. Breuer and F. Petruccione, *The theory of open quantum systems* (Oxford University Press, 2002).
- [16] Á. Rivas and S. F. Huelga, *Open Quantum Systems. An Introduction* (Springer Berlin Heidelberg, 2012).
- [17] U. Weiss, *Quantum dissipative systems* (World scientific, 2012).
- [18] D. Bacon, A. M. Childs, I. L. Chuang, J. Kempe, D. W. Leung, and X. Zhou, Universal simulation of Markovian quantum dynamics, *Phys. Rev. A* **64**, 062302 (2001).
- [19] S. Lloyd and L. Viola, Engineering quantum dynamics, *Phys. Rev. A* **65**, 010101 (2001).
- [20] M. Koniorczyk, V. Bužek, and P. Adam, Simulation of generators of Markovian dynamics on programmable quantum processors, *Eur. Phys. J. D* **37**, 275 (2006).
- [21] H. Wang, S. Ashhab, and F. Nori, Quantum algorithm for simulating the dynamics of an open quantum system, *Phys. Rev. A* **83**, 062317 (2011).
- [22] M. Kliesch, T. Barthel, C. Gogolin, M. Kastoryano, and J. Eisert, Dissipative Quantum Church-Turing Theorem, *Phys. Rev. Lett.* **107**, 120501 (2011).
- [23] M. Müller, S. Diehl, G. Pupillo, and P. Zoller, Engineered open systems and quantum simulations with atoms and ions, in *Advances in Atomic, Molecular, and Optical Physics*, Vol. 61, edited by P. Berman, E. Arimondo, and C. Lin (Academic Press, 2012) pp. 1–80.
- [24] R. Sweke, I. Sinayskiy, and F. Petruccione, Simulation of single-qubit open quantum systems, *Phys. Rev. A* **90**, 022331 (2014).
- [25] R. Sweke, I. Sinayskiy, D. Bernard, and F. Petruccione, Universal simulation of Markovian open quantum systems, *Phys. Rev. A* **91**, 062308 (2015).
- [26] S.-J. Wei, D. Ruan, and G.-L. Long, Duality quantum algorithm efficiently simulates open quantum systems, *Sci. Rep.* **6**, 30727 (2016).
- [27] P. Zanardi, J. Marshall, and L. Campos Venuti, Dissipative universal Lindbladian simulation, *Phys. Rev. A* **93**, 022312 (2016).
- [28] A. M. Childs and T. Li, Efficient simulation of sparse Markovian quantum dynamics, *Quantum Inf. Comput.* **17**, 901 (2016).
- [29] R. Cleve and C. Wang, Efficient Quantum Algorithms for Simulating Lindblad Evolution, in *44th Int. Colloq. Autom. Lang. Program. (ICALP 2017)* (2017) pp. 17:1–17:14.
- [30] S. Patsch, S. Maniscalco, and C. P. Koch, Simulation of open-quantum-system dynamics using the quantum Zeno effect, *Phys. Rev. Res.* **2**, 023133 (2020).
- [31] M. Cattaneo, G. De Chiara, S. Maniscalco, R. Zambrini, and G. L. Giorgi, Collision Models Can Efficiently Simulate Any Multipartite Markovian Quantum Dynamics, *Phys. Rev. Lett.* **126**, 130403 (2021).
- [32] H. Kamakari, S.-N. Sun, M. Motta, and A. J. Minnich, Digital quantum simulation of open quantum systems using quantum imaginary time evolution, preprint arXiv:2104.07823 (2021).
- [33] J. T. Barreiro, M. Müller, P. Schindler, D. Nigg, T. Monz, M. Chwalla, M. Hennrich, C. F. Roos, P. Zoller, and R. Blatt, An open-system quantum simulator with trapped ions, *Nature* **470**, 486 (2011).
- [34] P. Schindler, M. Müller, D. Nigg, J. T. Barreiro, E. A. Martinez, M. Hennrich, T. Monz, S. Diehl, P. Zoller, and R. Blatt, Quantum simulation of dynamical maps with trapped ions, *Nat. Phys.* **9**, 361 (2013).
- [35] G. García-Pérez, M. A. C. Rossi, and S. Maniscalco, IBM Q Experience as a versatile experimental testbed for simulating open quantum systems, *Npj Quantum Inf.* **6**, 1 (2020).
- [36] J. Han, W. Cai, L. Hu, X. Mu, Y. Ma, Y. Xu, W. Wang, H. Wang, Y. P. Song, C.-L. Zou, and L. Sun, Experimental Simulation of Open Quantum System Dynamics via Trotterization, *Phys. Rev. Lett.* **127**, 020504 (2021).
- [37] S. Tornow, W. Gehrke, and U. Helmbrecht, Non-Equilibrium Dynamics of a Dissipative Two-Site Hubbard Model Simulated on the IBM Quantum Computer, preprint arXiv:2011.11059 (2020).
- [38] P. P. Hofer, M. Perarnau-Llobet, L. D. M. Miranda, G. Haack, R. Silva, J. B. Brask, and N. Brunner, Markovian master equations for quantum thermal machines: local versus global approach, *New J. Phys.* **19**, 123037 (2017).
- [39] J. O. González, L. A. Correa, G. Nocerino, J. P. Palao, D. Alonso, and G. Adesso, Testing the Validity of the ‘Local’ and ‘Global’ GKLS Master Equations on an Exactly Solvable Model, *Open Syst. Inf. Dyn.* **24**, 1740010 (2017).
- [40] M. Cattaneo, G. L. Giorgi, S. Maniscalco, and R. Zambrini, Local versus global master equation with common and separate baths: superiority of the global approach in partial secular approximation, *New J. Phys.* **21**, 113045 (2019).
- [41] M. A. Nielsen and I. Chuang, *Quantum Computation and Quantum Information: 10th Anniversary Edition* (Cambridge University Press, 2010).
- [42] E. M. Kessler, G. Giedke, A. Imamoglu, S. F. Yelin, M. D. Lukin, and J. I. Cirac, Dissipative phase transition in a central spin system, *Phys. Rev. A* **86**, 012116 (2012).
- [43] G. L. Giorgi, F. Plastina, G. Francica, and R. Zambrini, Spontaneous synchronization and quantum correlation dynamics of open spin systems, *Phys. Rev. A* **88**, 042115 (2013).
- [44] S. Walter, A. Nunnenkamp, and C. Bruder, Quantum Synchronization of a Driven Self-Sustained Oscillator, *Phys. Rev. Lett.* **112**, 094102 (2014).
- [45] M. Xu, D. A. Tieri, E. C. Fine, J. K. Thompson, and M. J. Holland, Synchronization of Two Ensembles of

- Atoms, Phys. Rev. Lett. **113**, 154101 (2014).
- [46] H. Keßler, P. Kongkhambut, C. Georges, L. Mathey, J. G. Cosme, and A. Hemmerich, Observation of a Dissipative Time Crystal, Phys. Rev. Lett. **127**, 043602 (2021).
- [47] A. Levy and R. Kosloff, The local approach to quantum transport may violate the second law of thermodynamics, Europhys. Lett. **107**, 20004 (2014).
- [48] G. De Chiara, G. T. Landi, A. Hewgill, B. Reid, A. Ferraro, A. J. Roncaglia, and M. Antezza, Reconciliation of quantum local master equations with thermodynamics, New J. Phys. **20**, 113024 (2018).
- [49] F. Verstraete, M. M. Wolf, and J. Ignacio Cirac, Quantum computation and quantum-state engineering driven by dissipation, Nat. Phys. **5**, 633 (2009).
- [50] D. Braun, Creation of Entanglement by Interaction with a Common Heat Bath, Phys. Rev. Lett. **89**, 277901 (2002).
- [51] Y. Lin, J. P. Gaebler, F. Reiter, T. R. Tan, R. Bowler, A. S. Sørensen, D. Leibfried, and D. J. Wineland, Dissipative production of a maximally entangled steady state of two quantum bits, Nature **504**, 415 (2013).
- [52] M. E. Kimchi-Schwartz, L. Martin, E. Flurin, C. Aron, M. Kulkarni, H. E. Türeci, and I. Siddiqi, Stabilizing Entanglement via Symmetry-Selective Bath Engineering in Superconducting Qubits, Phys. Rev. Lett. **116**, 240503 (2016).
- [53] F. Caruso, A. W. Chin, A. Datta, S. F. Huelga, and M. B. Plenio, Entanglement and entangling power of the dynamics in light-harvesting complexes, Phys. Rev. A **81**, 062346 (2010).
- [54] M. Sarovar, T. Proctor, K. Rudinger, K. Young, E. Nielsen, and R. Blume-Kohout, Detecting crosstalk errors in quantum information processors, Quantum **4**, 321 (2020).
- [55] U. von Lüpke, F. Beaudoin, L. M. Norris, Y. Sung, R. Winik, J. Y. Qiu, M. Kjaergaard, D. Kim, J. Yoder, S. Gustavsson, L. Viola, and W. D. Oliver, Two-Qubit Spectroscopy of Spatiotemporally Correlated Quantum Noise in Superconducting Qubits, PRX Quantum **1**, 010305 (2020).
- [56] M. Gross and S. Haroche, Superradiance: An essay on the theory of collective spontaneous emission, Phys. Rep. **93**, 301 (1982).
- [57] A. Crubellier, S. Liberman, D. Pavolini, and P. Pillet, Superradiance and subradiance. I. Interatomic interference and symmetry properties in three-level systems, J. Phys. B: At. Mol. Opt. **18**, 3811 (1985).
- [58] S. Campbell and B. Vacchini, Collision models in open system dynamics: A versatile tool for deeper insights?, Europhys. Lett. **133**, 60001 (2021).
- [59] F. Ciccarello, S. Lorenzo, V. Giovannetti, and G. M. Palma, Quantum collision models: open system dynamics from repeated interactions, preprint arXiv:2106.11974 (2021).
- [60] F. Barra, The thermodynamic cost of driving quantum systems by their boundaries, Sci. Rep. **5**, 14873 (2015).
- [61] P. Strasberg, G. Schaller, T. Brandes, and M. Esposito, Quantum and Information Thermodynamics: A Unifying Framework Based on Repeated Interactions, Phys. Rev. X **7**, 021003 (2017).
- [62] S. Kretschmer, K. Luoma, and W. T. Strunz, Collision model for non-Markovian quantum dynamics, Phys. Rev. A **94**, 012106 (2016).
- [63] S. N. Filippov, J. Piilo, S. Maniscalco, and M. Ziman, Divisibility of quantum dynamical maps and collision models, Phys. Rev. A **96**, 032111 (2017).
- [64] Á. Cuevas, A. Geraledi, C. Liorni, L. D. Bonavena, A. De Pasquale, F. Sciarrino, V. Giovannetti, and P. Mataloni, All-optical implementation of collision-based evolutions of open quantum systems, Sci. Rep. **9**, 3205 (2019).
- [65] M. D. Sajid Anis *et al.*, Qiskit: An open-source framework for quantum computing (2021).
- [66] F. Leymann and J. Barzen, The bitter truth about gate-based quantum algorithms in the NISQ era, Quantum Sci. Technol. **5**, 044007 (2020).
- [67] E. Knill, D. Leibfried, R. Reichle, J. Britton, R. B. Blakestad, J. D. Jost, C. Langer, R. Ozeri, S. Seidelin, and D. J. Wineland, Randomized benchmarking of quantum gates, Phys. Rev. A **77**, 012307 (2008).
- [68] E. Magesan, R. Blume-Kohout, and J. Emerson, Gate fidelity fluctuations and quantum process invariants, Phys. Rev. A **84**, 012309 (2011).
- [69] E. Magesan, J. M. Gambetta, and J. Emerson, Scalable and Robust Randomized Benchmarking of Quantum Processes, Phys. Rev. Lett. **106**, 180504 (2011).
- [70] E. Magesan, J. M. Gambetta, B. R. Johnson, C. A. Ryan, J. M. Chow, S. T. Merkel, M. P. da Silva, G. A. Keefe, M. B. Rothwell, T. A. Ohki, M. B. Ketchen, and M. Steffen, Efficient Measurement of Quantum Gate Error by Interleaved Randomized Benchmarking, Phys. Rev. Lett. **109**, 080505 (2012).
- [71] E. Magesan, J. M. Gambetta, and J. Emerson, Characterizing quantum gates via randomized benchmarking, Phys. Rev. A **85**, 042311 (2012).
- [72] J. J. Wallman and S. T. Flammia, Randomized benchmarking with confidence, New J. Phys. **16**, 103032 (2014).
- [73] F. Arute *et al.*, Quantum supremacy using a programmable superconducting processor, Nature **574**, 505 (2019).
- [74] Y. Wu *et al.*, Strong Quantum Computational Advantage Using a Superconducting Quantum Processor, Phys. Rev. Lett. **127**, 180501 (2021).
- [75] A. Y. Kitaev, Quantum computations: algorithms and error correction, Russ. Math. Surv. **52**, 1191 (1997).
- [76] J. Watrous, *The Theory of Quantum Information* (Cambridge University Press, 2018).
- [77] A. Gilchrist, N. K. Langford, and M. A. Nielsen, Distance measures to compare real and ideal quantum processes, Phys. Rev. A **71**, 062310 (2005).
- [78] M. M. Wilde, *Quantum information theory* (Cambridge University Press, 2017).
- [79] A. Ben-Aroya and A. Ta-Shma, On the complexity of approximating the diamond norm, Quantum Inf. Comput. **10**, 77 (2010).
- [80] J. Watrous, Simpler semidefinite programs for completely bounded norms, preprint arXiv:1207.5726 (2012).
- [81] J. Watrous, John Watrous's Lecture Notes: Theory of Quantum Information (2011).
- [82] F. B. Maciejewski, Z. Puchała, and M. Oszmaniec, Operational quantum average-case distances, preprint arXiv:2112.14283 (2021).
- [83] J. Wallman, C. Granade, R. Harper, and S. T. Flammia, Estimating the coherence of noise, New J. Phys. **17**, 113020 (2015).



- [84] M. Bina, A. Mandarino, S. Olivares, and M. G. A. Paris, Drawbacks of the use of fidelity to assess quantum resources, *Phys. Rev. A* **89**, 012305 (2014).
- [85] D. Aharonov and M. Ben-Or, Fault-Tolerant Quantum Computation with Constant Error Rate, *SIAM J. Comput.* **38**, 1207 (2008).
- [86] Y. R. Sanders, J. J. Wallman, and B. C. Sanders, Bounding quantum gate error rate based on reported average fidelity, *New J. Phys.* **18**, 012002 (2015).
- [87] R. Kueng, D. M. Long, A. C. Doherty, and S. T. Flammia, Comparing Experiments to the Fault-Tolerance Threshold, *Phys. Rev. Lett.* **117**, 170502 (2016).
- [88] J. J. Wallman, Bounding experimental quantum error rates relative to fault-tolerant thresholds (2015).
- [89] Z. Chen *et al.*, Exponential suppression of bit or phase errors with cyclic error correction, *Nature* **595**, 383 (2021).
- [90] C. Ryan-Anderson *et al.*, Realization of real-time fault-tolerant quantum error correction, preprint arXiv:2107.07505 (2021).
- [91] R. Blume-Kohout, J. K. Gamble, E. Nielsen, K. Rudinger, J. Mizrahi, K. Fortier, and P. Maunz, Demonstration of qubit operations below a rigorous fault tolerance threshold with gate set tomography, *Nat. Commun.* **8**, 14485 (2017).
- [92] A. Carignan-Dugas, J. J. Wallman, and J. Emerson, Bounding the average gate fidelity of composite channels using the unitarity, *New J. Phys.* **21**, 053016 (2019).
- [93] Note that a universal bound for any  $m$  and  $\varphi$  cannot be found, because the average gate infidelity cannot be higher than 1.
- [94] N. Hatano and M. Suzuki, Finding Exponential Product Formulas of Higher Orders, in *Quantum Annealing and Other Optimization Methods* (Springer, 2005) pp. 37–68.
- [95] B. Bellomo, G. L. Giorgi, G. M. Palma, and R. Zambrini, Quantum synchronization as a local signature of super- and subradiance, *Phys. Rev. A* **95**, 043807 (2017).
- [96] M. Cattaneo, G. L. Giorgi, S. Maniscalco, G. S. Paroanu, and R. Zambrini, Bath-Induced Collective Phenomena on Superconducting Qubits: Synchronization, Subradiance, and Entanglement Generation, *Ann. Phys. (Berlin)* **533**, 2100038 (2021).
- [97] D. A. Lidar and K. Birgitta Whaley, Decoherence-free subspaces and subsystems, in *Irreversible Quantum Dynamics* (2003) pp. 83–120.
- [98] S. Lorenzo, F. Ciccarello, and G. M. Palma, Composite quantum collision models, *Phys. Rev. A* **96**, 032107 (2017).
- [99] M.-D. Choi, Completely positive linear maps on complex matrices, *Linear Algebra Its Appl.* **10**, 285 (1975).
- [100] D. Willsch, M. Nocon, F. Jin, H. De Raedt, and K. Michielsen, Gate-error analysis in simulations of quantum computers with transmon qubits, *Phys. Rev. A* **96**, 062302 (2017).
- [101] K. Michielsen, M. Nocon, D. Willsch, F. Jin, T. Lippert, and H. De Raedt, Benchmarking gate-based quantum computers, *Comput. Phys. Commun.* **220**, 44 (2017).
- [102] D. Bultrini, M. H. Gordon, E. López, and G. Sierra, Simple Mitigation Strategy for a Systematic Gate Error in IBMQ, *Journal of Applied Mathematics and Physics* **09**, 1215 (2021).
- [103] A. Carignan-Dugas, K. Boone, J. J. Wallman, and J. Emerson, From randomized benchmarking experiments to gate-set circuit fidelity: how to interpret randomized benchmarking decay parameters, *New J. Phys.* **20**, 092001 (2018).
- [104] J. J. Wallman, Randomized benchmarking with gate-dependent noise, *Quantum* **2**, 47 (2018).
- [105] A. Carignan-Dugas, *A walk through quantum noise: a study of error signatures and characterization methods*, Ph.D. thesis, University of Waterloo (2019).
- [106] T. Proctor, K. Rudinger, K. Young, M. Sarovar, and R. Blume-Kohout, What Randomized Benchmarking Actually Measures, *Phys. Rev. Lett.* **119**, 130502 (2017).
- [107] J. Qi and H. K. Ng, Comparing the randomized benchmarking figure with the average infidelity of a quantum gate-set, *Int. J. Quantum Inf.* **17**, 1950031 (2019).
- [108] T. Alexander, N. Kanazawa, D. J. Egger, L. Capelluto, C. J. Wood, A. Javadi-Abhari, and D. C McKay, Qiskit pulse: programming quantum computers through the cloud with pulses, *Quantum Sci. Technol.* **5**, 044006 (2020).
- [109] J. P. Stenger, N. T. Bronn, D. J. Egger, and D. Pekker, Simulating the dynamics of braiding of majorana zero modes using an ibm quantum computer, *Phys. Rev. Research* **3**, 033171 (2021).
- [110] S. Lang, *Algebra* (Springer-Verlag, 2002).
- [111] A. H. Werner, D. Jaschke, P. Silvi, M. Kliesch, T. Calarco, J. Eisert, and S. Montangero, Positive Tensor Network Approach for Simulating Open Quantum Many-Body Systems, *Phys. Rev. Lett.* **116**, 237201 (2016).
- [112] D. A. Lidar, P. Zanardi, and K. Khodjasteh, Distance bounds on quantum dynamics, *Phys. Rev. A* **78**, 012308 (2008).
- [113] J. Johansson, P. Nation, and F. Nori, QuTiP: An open-source Python framework for the dynamics of open quantum systems, *Comput. Phys. Commun.* **183**, 1760 (2012).